

1 2 9 0



UNIVERSIDADE D
COIMBRA

João Miguel Sameiro Dias

A STUDY ON BENDING STIFFNESS
CHARACTERIZATION OF BIOHYBRID
MICROROBOTS USING EXTERNAL
MAGNETIC ACTUATION

Dissertation for Integrated Master's Degree in Biomedical Engineering under
the supervision of Professor Lino Marques and Professor Islam S. M. Khalil
and presented to the University of Coimbra

October, 2021

University of Coimbra
Faculty of Sciences and Technology

A Study on Bending Stiffness Characterization of Biohybrid Microrobots using External Magnetic Actuation

João Miguel Sameiro Dias

Dissertation presented to the Department of Physics of the Faculty of Sciences and
Technology of the University of Coimbra

Supervisors:

Professor Doctor Lino Marques (DEEC/UC)

Professor Doctor Islam S. M. Khalil (DBE/UT)

Coimbra, 2021



UNIVERSIDADE D
COIMBRA

O presente trabalho foi realizado com a colaboração de um grupo internacional e multidisciplinar de investigadores e foi submetido para publicação na revista: *Advanced Theory and Simulations*.

The present work was accomplished through the collaboration of an international and multidisciplinary group of people and is currently being reviewed to publishing in the journal: *Advanced Theory and Simulations*.

ACKNOWLEDGEMENTS

It began uncertain, the path towards my future, but was soon very clear in my mind what it was, and this work marks the end of one of the most beautiful chapters of my life. So many things happened, so many moments happened and important ones, therefore I feel that it is of the utmost importance that I take this opportunity to recollect and appreciate all that made this possible.

I will start with the most formal acknowledgments:

First, to my university colleagues – through the many groupworks, classes, and time together, thank you for keeping up with me, I know I was not always the best person to work with, but I am sure our time together taught us the experience we need to find our way through life.

To my professors – for making me learn so many things I thought it was impossible. Some more than others, I was lucky to find amazing and caring teachers in the Department of Physics and other departments, so thank you for your attitude towards the students, I am sure the next to come will have a great time with you.

A special acknowledgment to the team that made this research project possible:

To Dr. Julliane Simmchen from the Physical Chemistry and Electrochemistry Department at Technical University of Dresden for providing the experiment samples through the most complicated times, some never reached me, but you were tireless in always providing me the best samples you could make.

To Dr. Anke Klingner from the Physics Department at the German University in Cairo and Dr. David Smith from the School of Mathematics at the University of Birmingham, thank you for providing all the theoretical and mathematical models that are described in this project and ultimately resulted in the best simulation results.

And finally, to Dr. Veronika Magdanz from the Institute for Bioengineering of Catalonia, thank you for your time in all our meetings and for always being present in important discussions, crucial to the development of this project.

To my supervisors – Prof. Dr. Lino Marques for caring and helping me during this thesis even though we were separated by over two thousand kilometres. Thank you for your comments, your patience, and your committal to this project. To my supervisor in The Netherlands, Prof. Dr. Islam Khalil from the Surgical Robotics Laboratory at the University of Twente, thank you for getting me in the world of

microrobotics, for teaching me its basics, for always having time for answering my questions and doubts, and for also motivating me through this past year. You are an incredible person, and I will never forget this experience I had with you. Thank you.

And now the more affectional acknowledgments will go for the following:

To my friends back home – Ilca, Cláudia, Kika, Carlos, Sousa, and Vitor... Sometimes I don't feel like I deserve your friendship, but despite all the weekends I could not hang out with you, you always met me with joy on our rare meetings. Either way, I know we all love each other, and it is because of our friendship that no matter how far we are, or how long we are not together, we can all find in each other a home.

To my “Coimbra friends” – Erica, Marli, Joana, Pipa, Berto, Luís, Luís, Tiago, Tiago, Rute, Samuel, Catarina, Diogo, Matos, Simão, Júlio, Miguel, Botas, António, Vasco, Carlota, Raquel, Paz, Marta, Mariana, Joana, and so many others... We lived so many adventures during these 6 years of my life, I can never thank you for them all. Coimbra is now another place I can call home and it is also thanks to you people.

To Berto and Camilo – our journey as university colleagues was short, but our friendship remains despite the distance of our conversations and rare time together. Nevertheless, I know we can always find each other for more great conversations and time together in the years to come, and I pray that our paths keep crossing with each other.

To everyone I met on extracurricular activities during this journey – namely, DG/AAC, COQF, CUC, ATACÓPITO, BEST, NEDF/AAC – working in a team full of different thinking people is by far the best way to evolve professionally, so thank you for teaching me and also allow me to lead some of you in all of our projects together. I met so many great friends through these opportunities, we've had so much fun, and more chances will come to spend more time together, either work or leisure.

To Twente – an amazing international experience that I will never forget. Although Covid put a break on a lot of things, I met incredible people, had amazing experiences, and I got home with a heart full of amazing moments.

To Coimbra – the city of students – a city full of culture, tradition, and history. Thank you for receiving me with open arms, for letting me walk through your beautiful and characteristic streets, for the great environment you provided so that I could meet the most incredible friends, and finally, the best of all the things you

give every student that has the luck to call you home, another family to love and cherish. Even though I could talk about you for eons, I will never find the right words to describe the love I have for you, the gratitude I have towards you, but I will leave here a verse that most resembles such emotion: “Coimbra, ai quem me dera parar o tempo e ficar, dos teus braços vejo o mundo, sem pressa de embarcar.”

To “os Borgas” – my Coimbra family – to the ones that came before me and I had the pleasure to meet: Gouveia, Mauro, Gonçalo e Chico, I found in all of you values to learn and respect, traditions to keep, but most importantly a family, I will never be able to thank you enough for all your teachings. To PJ, my “godfather”, my pillar in my first year in a unknown city, thank you for teaching me all you knew, for our time together, I hope we meet many more times in the future, and most importantly, for unknowingly spark the creation of the greatest ‘família de praxe’ to ever exist in this University. To the ones that came next: Artur, André, and Jorge for being the first ones embarking in what is a growing group of individuals full of energy, diversity, with a constant thirst for beer, hence the name, and most importantly, full of love, respect, honesty, and friendship. And to the ones that came next: Alexandre and Gonçalo, and later: Afonso and Eduardo, thank you for excellently learning the values that our family holds and for always making sure that this legacy will last, at least I hope so. All of you are the very definition of the verse from our dear song “Balada da Despedida do 5º Ano Jurídico” – “Levo comigo prá vida” and I will, to the best of my capabilities, take you in my heart for the rest of my life.

To those not mentioned, rest assured, I have not forgotten you, because you also had an impact on these years of my life. I live my life learning whatever I can from each and every interaction with everyone, so only crossing our paths together is enough to leave a mark in my journey and I am forever thankful for those moments.

And finally, to my parents and family – the ultimate heroes that allowed this 6-year adventure to reach its end, for financing the majority of my studies, but more importantly, for always being my anchor to the place I can call home.

ABSTRACT

Microrobotics is rapidly becoming a key instrument in various medical interventions that were previously thought to be impossible. With its reduced size, delivering clinical treatment in difficult-to-reach areas of our body without damaging healthy organs and tissues is now a thing of the past. Despite these great technological achievements, there are several hurdles such as locomotion and localization mechanisms we must surpass to achieve a perfect microrobot capable of performing desired tasks without major complications.

A microrobot called IRONSperm capable of swimming in low- Re conditions and achieve targeted drug delivery was designed by merging bull sperm cells with magnetic nanoparticles that create several coating patterns along the cell's flagella enabling transportation by application of external magnetic fields. This untethered microswimmer achieves propulsion by actuating a traveling wave along its flexible tail and the bending stiffness is the only intrinsic property that governs the form and rate of wave propagation along its length.

In this work, it is studied the effects of the magnetic coating on an intrinsic physical property of the flagella called passive bending stiffness. Furthermore, the efficiency of the electromagnetic system used to calculate such property is also evaluated. Theoretical and experimental results then proved that the presence of nanoparticles attached to the tail of sperm cells highly influences its bending stiffness. It was also found that the bending stiffness is proportional to the number and location of magnetized cellular segments, reaching minimum values of $3.79 \times 10^{-21} \text{ N} \cdot \text{m}^2$ for flagella with one magnetized cellular segment, and maximum values up to $16.6 \times 10^{-21} \text{ N} \cdot \text{m}^2$ for fully coated flagella microswimmers.

KEYWORDS: minimal invasive medical techniques, microrobotics, soft robots, bending stiffness, flagellar propulsion, magnetic actuation

RESUMO

A microrrobótica está rapidamente a tornar-se um instrumento-chave em várias intervenções médicas que antes eram consideradas impossíveis. Com seu tamanho reduzido, fornecer tratamento clínico em zonas de difícil acesso do nosso corpo sem danificar órgãos e tecidos saudáveis é agora uma coisa do passado. Apesar destas grandes conquistas tecnológicas, existem vários obstáculos como mecanismos de locomoção e localização que devemos ultrapassar para alcançar um microrrobot perfeito, capaz de realizar tarefas desejadas sem grandes complicações.

Um microrrobot chamado IRONSperm capaz de nadar em condições de *low-Re* e alcançar a administração de drogas foi projetado pela fusão de células de espermatozoides com nanopartículas magnéticas que criam vários padrões de revestimento ao longo dos flagelos da célula, permitindo o transporte por aplicação de campos magnéticos externos. Este microrrobot sem fios alcança a propulsão atuando uma onda viajante ao longo de sua cauda flexível e a rigidez de flexão é a única propriedade intrínseca que governa a forma e a taxa de propagação da onda ao longo de seu comprimento.

Neste trabalho, são estudados os efeitos do revestimento magnético sobre uma propriedade física intrínseca dos flagelos denominada rigidez de flexão passiva. Além disso, a eficiência do sistema eletromagnético utilizado para calcular tal propriedade também é avaliada. Resultados teóricos e experimentais provaram que a presença de nanopartículas aderidas à cauda dos espermatozoides influenciam fortemente sua rigidez de flexão. Também foi descoberto que a rigidez de flexão é proporcional à quantidade e localização dos segmentos celulares magnetizados, atingindo valores mínimos de $3.79 \times 10^{-21} \text{ N.m}^2$ para flagelos com um segmento celular magnetizado e valores máximos até $16,6 \times 10^{-21} \text{ N.m}^2$ para micro-nadadores em que o flagelo se encontra totalmente revestido com nanopartículas.

PALAVRAS-CHAVE: técnicas médicas minimamente invasivas, microrrobótica, robots soft, rigidez de flexão, propulsão flagelar, atuação magnética

LIST OF FIGURES

FIGURE 1 Visual representation of helical propulsion (a) and transverse-wave propulsion (b) of soft microrobots. Adapted from Nelson et al. (2010)[3]..... 3

FIGURE 2 Illustration of the forces applied on a segment δs when moving transversely across the axis of progression xx . (A) At velocity Vy , the resultant propulsive thrust is $\delta F_{\perp} = \delta Ny \sin\theta - \delta Ly \cos\theta$, where δNy and δLy are the reactions from the fluid acting normally and tangentially to the surface of the segment, and θ is the angle of inclination of the segment to the axis xx . (B) At velocity Vx , the resultant propulsive thrust is $\delta F_{\parallel} = \delta Nx \sin\theta + \delta Lx \cos\theta$. The net propulsive thrust is then a combination of these two, thus giving Equation 2. Adapted from Gray et al. (1955)[16]..... 4

FIGURE 3 Different flagellar wave patterns and propulsive thrust for corresponding Sperm numbers. The graphic in the figure shows the peak for propulsive force is reached at a $Sp = 2.1$. Adapted from Khalil et al. (2020)[18]..... 5

FIGURE 4 Microscopic images of dead bovine sperm cells coated with maghemite nanoparticles with different assembly sites. (a) normal sperm cell. (b) distal piece coated. (c) principal piece coated. (d) midpiece coated. (e) principal and distal pieces coated. (f) midpiece and distal piece coated. (g) midpiece and principal piece coated. (h) fully coated. Adapted from Magdanz et al. (2021) [69]. 16

FIGURE 5 The bending stiffness varies along the flagellum due to a change in moment of area, $I(m, p, d, x)$, and elastic modulus, $E(m, p, d, x)$. (a) It tapers gradually toward the distal end with a taper factor f . (b) The location of the magnetizable cellular segment is determined during electrostatic self-assembly and the indices m, p, d designate the magnetized region. (c) The applied field, B , produces elastic deformation of the flagellum using magnetic torque exerted on its dipole moment. (d) The elastic bending resistance of the passive flagellum is balanced by the viscous drag in the surrounding fluid when the applied field is removed, $B = 0$. Adapted from Magdanz et al. (2021) [69]..... 19

FIGURE 6 Experimental setup illustration. (a) camera. (b) image filter. (c) 3D-printed coil holder. (d) Plexiglas disk do hold sample laminas. (e) supporting semi-circular wedge. (f) electromagnetic coil. 22

FIGURE 7 Representation of the applied external magnetic field. (a) The magnetic fields of each coil are superimposed and controlled to dynamically excite the

flagellum. (b) Field strength of 5 mT is applied at the position of the flagellum marked as the black dot. Adapted from Magdanz et al. (2021) [69]. 23

FIGURE 8 Four different cantilever structures that were printed using 2PL technology with posterior magnetic coating for external actuation. Of them all, the cantilever (a) showed more similarities to coated sperm cells. (a), (b), and (d) have $2\mu m$ diameter radius, and (c) has $1\mu m$ diameter radius. 24

FIGURE 9 The absolute values of the determinant of M are calculated versus r_m (m,p,d) for all groups. (a) For a fully uncoated and fully coated flagella. (b) For distal coated, principal piece coated, and midpiece coated flagella. (c) For flagella with two coated cellular segments. Adapted from Magdanz et al. (2021) [69]. 25

FIGURE 10 Simulation results for (0,0,0) (a)–(d) and (1,1,1) (e)–(h) configurations. Since there is no magnetic particles in the uncoated flagella, the distal end is considered dragged by a contact force and then removed so that the elastic moment restores it to the original position (a)–(b). Adapted from Magdanz et al. (2021) [69]. 27

FIGURE 11 Simulation results for (0,0,1) (a)–(d), (0,1,0) (e)–(h) and (1,0,0) (i)–(l) configurations. Adapted from Magdanz et al. (2021) [69]. 29

FIGURE 12 Simulation results for (0,1,1) (a)–(d), (1,0,1) (e)–(h), and (1,1,0) (i)–(l) configurations. Adapted from Magdanz et al. (2021) [69]. 31

FIGURE 13 Actuation frequency, ω , of a magnetizable segment is calculated for different bending stiffness, κ , and sperm number, Sp , using Equation (4). (a) For optimal flagellar propulsion ($Sp = 2.1$), the optimal actuation frequency is directly proportional to the averaged bending stiffness over the length. (b) Optimal propulsive time-averaged thrust force, f , of a flagellum with greater bending stiffness is achieved at higher actuation frequency [68]. Improvement of the frequency response is achieved for flagellum with greater bending stiffness. Adapted from Magdanz *et al.* (2021) [69]. 32

FIGURE 14 Nanoparticle coated sperm cell with its head fixed to a solid boundary is actuated. At $t = 0 s$, the applied magnetic field is removed, and the flagellum restores to its original position. Adapted from Magdanz et al. (2021) [69]. 33

FIGURE 15 Bar plot with summarized results for Simulation 1 using Equations (11) and (27), Simulation 2 with Equation (28), measured bending stiffness using Equation (27), and reference value from [70]. 34

LIST OF TABLES

TABLE 1 Summarized table of the results with relaxation time, $\tau[s]$, and average bending stiffness, $\langle\kappa\rangle[N.m^2]$, of the various possible configurations of nanoparticle coated sperm cells with their correspondents standard deviations.	34
TABLE(A) 1 Summarized data extracted from experiment 16 with H001 configuration. With length, $L[\mu m]$, relaxation time, $\tau[s]$, and average bending stiffness, $\kappa[N.m^2]$, and their respective standard deviations.....	44
TABLE(A) 2 Data extracted from experiment 16. Sample with H001 configuration, where 10 trials were realized for 4 theta excitation angles, $\theta[^\circ]$, at $B = 5 mT$	44
TABLE(A) 3 Summarized data extracted from experiments 6, 13, 14, and 23 with H010 configuration. With length, $L[\mu m]$, relaxation time, $\tau[s]$, and average bending stiffness, $\langle\kappa\rangle[N.m^2]$, and their respective standard deviations.....	44
TABLE(A) 4 Data extracted from experiment 6. Sample with H010 configuration, where 10 trials were realized for 3 theta excitation angles, $\theta[^\circ]$, at $B = 5 mT$	45
TABLE(A) 5 Data extracted from experiment 13. Sample with H010 configuration, where 10 trials were realized for 4 theta excitation angles, $\theta[^\circ]$, at $B = 5 mT$	45
TABLE(A) 6 Data extracted from experiment 14. Sample with H010 configuration, where 10 trials were realized for 4 theta excitation angles, $\theta[^\circ]$, at $B = 5 mT$	46
TABLE(A) 7 Data extracted from experiment 23. Sample with H010 configuration, where 8 trials were realized for 3 theta excitation angles, $\theta[^\circ]$, at $B = 5 mT$	46
TABLE(A) 8 Summarized data extracted from experiments 19 and 20 with H100 configuration. With length, $L[\mu m]$, relaxation time, $\tau[s]$, and average bending stiffness, $\langle\kappa\rangle[N.m^2]$, and their respective standard deviations.....	46
TABLE(A) 9 Data extracted from experiment 19. Sample with H100 configuration, where 10 trials were realized for 1 theta excitation angle, $\theta[^\circ]$, at $B = 5 mT$	47
TABLE(A) 10 Data extracted from experiment 20. Sample with H100 configuration, where 10 trials were realized for 3 theta excitation angles, $\theta[^\circ]$, at $B = 5 mT$	47
TABLE(A) 11 Summarized data extracted from experiments 4, 11, 12, and 20 with H011 configuration. With length, $L[\mu m]$, relaxation time, $\tau[s]$, and average bending stiffness, $\kappa[N.m^2]$, and their respective standard deviations.....	47
TABLE(A) 12 Data extracted from experiment 4. Sample with H011 configuration, where 10 trials were realized for 3 theta excitation angle, $\theta[^\circ]$, at $B = 5 mT$	48

TABLE(A) 13 Data extracted from experiment 15. Sample with H011 configuration, where 10 trials were realized for 4 theta excitation angle, $\theta[^\circ]$, at $B = 5 \text{ mT}$ 48

TABLE(A) 14 Summarized data extracted from experiments 8 and 24 with H101 configuration. With length, $L[\mu\text{m}]$, relaxation time, $\tau[\text{s}]$, and average bending stiffness, $\langle\kappa\rangle[N. \text{m}^2]$, and their respective standard deviations..... 48

TABLE(A) 15 Data extracted from experiment 8. Sample with H101 configuration, where 10 trials were realized for 1 theta excitation angle, $\theta[^\circ]$, at $B = 5 \text{ mT}$ 49

TABLE(A) 16 Data extracted from experiment 24. Sample with H101 configuration, where 10 trials were realized for 3 theta excitation angle, $\theta[^\circ]$, at $B = 5 \text{ mT}$ 49

TABLE(A) 17 Summarized data extracted from experiments 18 and 22 with H110 configuration. With length, $L[\mu\text{m}]$, relaxation time, $\tau[\text{s}]$, and average bending stiffness, $\langle\kappa\rangle[N. \text{m}^2]$, and their respective standard deviations..... 49

TABLE(A) 18 Data extracted from experiment 18. Sample with H110 configuration, where 10 trials were realized for 1 theta excitation angle, $\theta[^\circ]$, at $B = 5 \text{ mT}$ 50

TABLE(A) 19 Data extracted from experiment 22. Sample with H110 configuration, where 3 and 6 trials were realized for 2 theta excitation angle, $\theta[^\circ]$, at $B = 5 \text{ mT}$. 50

TABLE(A) 20 Summarized data extracted from experiments 3, 5, 7, and 17 with H111 configuration. With length, $L[\mu\text{m}]$, relaxation time, $\tau[\text{s}]$, and average bending stiffness, $\kappa[N. \text{m}^2]$, and their respective standard deviations..... 50

TABLE(A) 21 Data extracted from experiment 17. Sample with H111 configuration, where 10 trials were realized for 3 theta excitation angle, $\theta[^\circ]$, at $B = 5 \text{ mT}$ 51

TABLE(A) 22 Data extracted from experiment 5. Sample with H111 configuration, where 10 trials were realized for 4 theta excitation angle, $\theta[^\circ]$, at $B = 5 \text{ mT}$ 51

TABLE(A) 23 Data extracted from experiment 3. Sample with H111 configuration, where 10 trials were realized for 5 theta excitation angle, $\theta[^\circ]$, at $B = 5 \text{ mT}$ 51

INDEX

Acknowledgements.....	i
Abstract.....	v
Resumo	vi
List Of Figures	vii
List Of Tables	ix
Index	xi
Chapter 1 – Introduction.....	1
1.1 Microrobotics.....	1
Fabrication.....	1
Locomotion/Powering.....	2
Localization	6
Impact/Applications	7
1.2 State Of The Art.....	8
Microrobots Designs	8
Bending Stiffness Determination Mechanisms.....	11
1.3 Motivation.....	13
Objectives.....	14
Chapter 2 – Materials And Methods	15
2.1 Microswimmer Fabrication.....	15
2.2 Bending Stiffness Estimation.....	16
Nanoparticle Coated Soft Flagellum	16
Magnetized Cellular Segments In A Magnetic Field.....	18
Relaxation Method.....	18
2.3 Experimental Setup	22
2.4 Control Group	24
Chapter 3 – Results.....	25
3.1 Simulation Results	25
Actuation Frequency.....	32
3.2 Experimental Results.....	33
Chapter 4 – Conclusion	36
References	37
Appendices	43
Appendix A – Tables.....	44

CHAPTER 1 – INTRODUCTION

In this first chapter, an introduction to the microrobotics field will be presented as well as a state of the art containing studies of relevant importance to the development of this work. Finally, at the end of the chapter, an overview of the objectives and motives that support the need for this research project is presented.

1.1 MICROROBOTICS

Medical interventions have been evolving in order to get better surgical outcomes, higher health benefits, and increased life expectancy [1]. One of the most promising fields of investigation when it comes to Medical Applications is Microrobotics, more specifically: microrobotics for minimal invasive medical applications. Compared to conventional robots with their large mechanical components, these untethered microscopic robots hold substantial promise for interventions like targeted drug delivery, cellular level surgeries, biosensing, cellular and tissue manipulation [1,2].

Flexible microrobots can navigate through natural pathways, perform noninvasive operations with gentle interaction with the surrounding tissue and at the same time maintain a high level of control and propulsion [2]. With so much potential within them, microrobots are most certainly the best concept to do tasks that are currently hard or impossible to perform due to environmental constraints such as difficult-to-reach areas or targeted therapies [3].

FABRICATION

The world of microrobotics is as enormous as the countless possibilities when it comes to their fabrication processes. These fabrication processes can be divided into two groups: artificial microrobots and biohybrid microrobots, which are basically a combination of biological and mechanical components [4].

Artificial microrobots face the most challenges as the microscopic world works differently from the world we are used to observe. Technology is not sufficiently developed enough to face the restrictions of the microscale world: chips and batteries are not sufficiently small to work properly in such environments and proper locomotion is still hard to achieve [5].

Biohybrid-made microrobots, on the other hand, can incorporate features from already existing microorganisms, like flagellum or capsules. They can serve off its structural component, on-board energy source and ways of locomotion to surpass already referred physical constraints and use the artificial components as means of sensing and localization by non-invasive imaging systems [6].

LOCOMOTION/POWERING

Although the fundamental physics governing both types of microrobots remain the same, and as already mentioned, life at the micro scale is different as the relative importance of physical properties such as fluid viscosity, surface area effects and electrostatic forces play the dominant role over the device's size, volume, and weight [7].

Nevertheless, Nature has found numerous ways to pass through these hurdles, so microorganisms provide inspirational ideas on how to move in such fluidic conditions. The world at microscale is either very viscous, very slow, or very small, and in such conditions, time becomes a negligible variable, the existence of walls becomes increasingly important and movement patterns becomes unchangeable [8].

The viscosity of a fluid can be characterized by its Reynolds number, which is defined as follow:

$$Re = \frac{UL}{\nu} \quad (1)$$

where U is a characteristic velocity, L is a length scale, and ν is the fluids kinematic viscosity. This microworld is known as a low Reynolds number fluid (low- Re) and here, low- Re stands for $Re < 1$ and inertial forces are negligible [9].

The length scale in these conditions is usually small ($\sim \mu m$) and linear viscous forces normally dominate over nonlinear inertial forces. So, in the case of absence of inertia, $Re \rightarrow 0$, the equations of motion become time-reversible, and any net movement gained by the swimmer must result in nonreciprocal motion, in other words, back and forth motion produces negligible net movement [9].

Nonetheless, Nature evolved strategies that enable microorganisms to swim in such conditions: helical propulsion using a rotating movement and traveling wave propulsion through actuation of flexible tail [10,11].

A large number of bacteria swim using a helical propeller mechanism by rotating a flexible passive flagellum. Although the creation of an artificial system that can swim in these conditions is quite difficult, recent studies have been successful in creating such traveling mechanism using external magnetic fields to induce rotating torque on flagella. These flagella can be rigid or partially rigid, or achieve a helical geometry only dynamically, but no matter the approach chosen, this helical propulsion mechanism provides an effective method to move through the lumens of a complex organism [11].

Being more efficient than helical propulsion, traveling waves are very effective to move through low- Re fluids, assuming an equal actuation frequency. This strategy adopted by eukaryotic microswimmers' flagella is very difficult to reproduce artificially raising problems in terms of fabrication, power, and control [12].

Despite these difficulties, various methods to replicate this mechanism are being used and perfected, as most of them work perfectly at bit bigger dimensions than the ones found at microscale. Such methods include using piezoelectric actuators distributed along a flagellum producing a push and pull movement [13]; distribution of electrically conducting coils along the length of the propeller [14]; and the use of an elastic tail as a propeller, similar to spermatozoa [15].

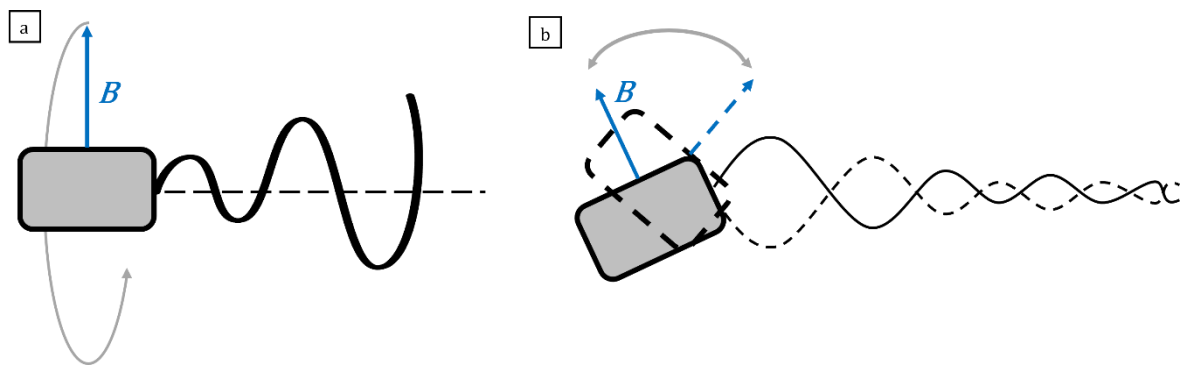


FIGURE 1 Visual representation of helical propulsion (a) and transverse-wave propulsion (b) of soft microrobots. Adapted from Nelson *et al.* (2010)[3].

This latter strategy of propulsion is the one that the microrobot presented in this work was inspired on, since it is a hybrid microrobot where its biological part consists of bull sperm cells. The physics behind the propulsion of this type of swimmers is very well explained by a theory proposed by Gray and Hancock in 1958 called Resistive Force Theory (RFT) [16].

In sum, propulsive thrust F can be given by:

$$\langle F \rangle = \int_0^L (F_{\parallel} + F_{\perp}) ds = \int_0^L (v_{\parallel}(s, t)\xi_{\parallel} + v_{\perp}(s, t)\xi_{\perp}) ds \quad (2)$$

$$\xi_{\parallel} = \frac{2\pi\eta}{\ln\left(\frac{L}{r}\right) - 0.807}; \quad \xi_{\perp} = \frac{2\pi\eta}{\ln\left(\frac{L}{r}\right) - 0.807} \quad (3)$$

where L is the length of the tail, v is the propulsion velocity, ξ is the drag coefficient, r is the mean radius of the sperm tail, and η the viscosity of the fluid medium [17]. This force propulsion is given by compensating of the effect of all the tangential forces acting along the body with propulsive components of forces acting normally along the surface of the body. The RFT assumes that the deforming body can be divided into small segments, each one experiencing drag and that the flow and force fields from these segments are hydrodynamically decoupled and do not influence the other segments' fields. Thus, the normal and tangential forces on a small segment δs , represented in

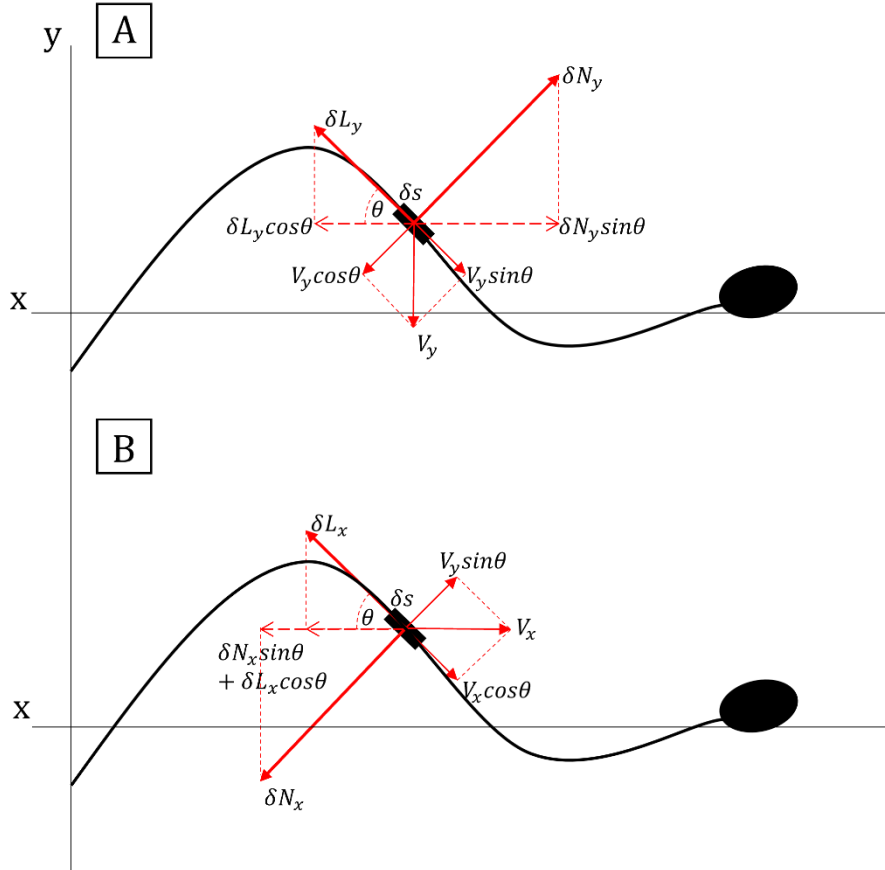


FIGURE 2 Illustration of the forces applied on a segment δs when moving transversely across the axis of progression xx . (A) At velocity V_y , the resultant propulsive thrust is $\delta F_{\perp} = \delta N_y \sin \theta - \delta L_y \cos \theta$, where δN_y and δL_y are the reactions from the fluid acting normally and tangentially to the surface of the segment, and θ is the angle of inclination of the segment to the axis xx . (B) At velocity V_x , the resultant propulsive thrust is $\delta F_{\parallel} = \delta N_x \sin \theta + \delta L_x \cos \theta$. The net propulsive thrust is then a combination of these two, thus giving Equation 2. Adapted from *Gray et al.* (1955)[16].

Figure 2, depend only on the local properties like the length of the segment, velocity, and orientation. This theory provides an excellent approximation of locomotion in viscous fluids since they have a complex flow dynamics and moving boundaries.

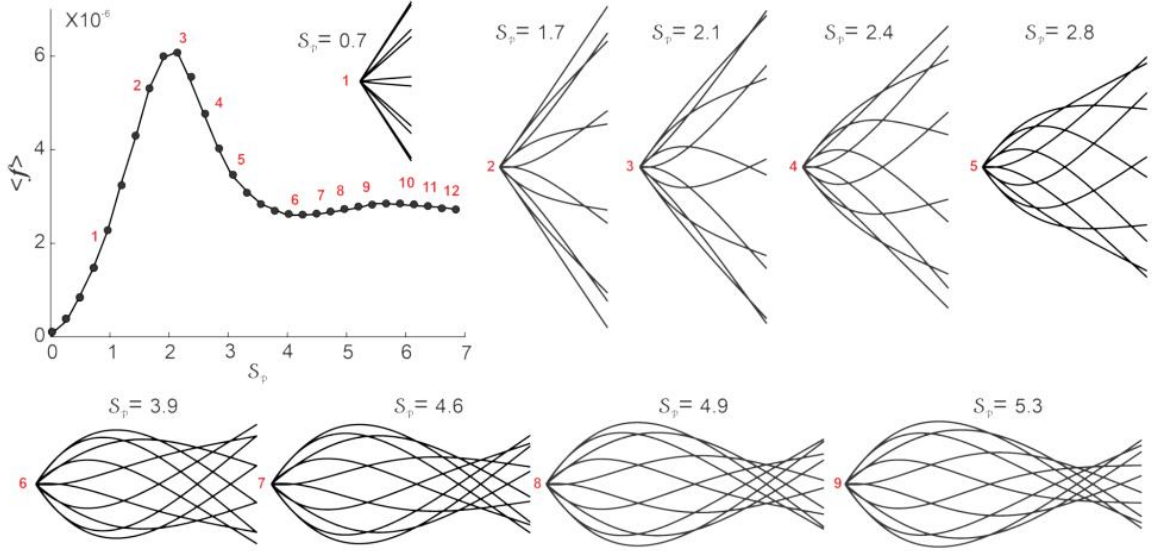


FIGURE 3 Different flagellar wave patterns and propulsive thrust for corresponding Sperm numbers. The graphic in the figure shows the peak for propulsive force is reached at a $Sp = 2.1$. Adapted from Khalil *et al.* (2020)[18].

A device's elastic tail has ideal properties: a short and rigid propeller will result in reduced net propulsion, and, conversely, if the propeller is too long and flexible there is an increase in drag relative to propulsion resulting in reduced net propulsion [3]. Yu *et al.* classified these ideal properties as Sperm number (Sp), in other words, they found optimal values for length, stiffness, and frequency, combining them and obtaining an optimal floppiness [15]. This dimensionless Sperm number is given by:

$$Sp = l \left(\frac{|\omega| \xi_{\perp}}{\kappa} \right)^{\frac{1}{4}} \quad (4)$$

where here l is the length of the tail, κ is the bending stiffness, ω is the rotational velocity, and ξ_{\perp} is the drag coefficient for flow perpendicular to the tail. As shown in Figure 3, they report an optimal value of $Sp = 2.1$, and they also find a fine agreement between theoretical, numerical, and experimental results.

Other locomotion strategies include the use of magnetic field gradients and clinical magnetic resonance imaging systems. Magnetic fields have been used in medicine for quite some time and when it comes to applying these fields to objects, this can be done in various ways: using position and current controlled electromagnets[19], ferromagnetic beads [20,21], permanent magnet beads controlled by electromagnetic

coils [22], helmet system composed of 3 orthogonal pairs of coils [23], position controlled permanent magnets for steering tools [24], and more and more continue to be developed. Attached nanoparticles can also be used to be controlled by magnetic field gradients which is the method used in controlling IRONSperms [25] and in the microrobot presented in this work, which is basically a variation of the former.

Finally, another approach on locomotion strategies for microrobots is the use of a clinical Magnetic Resonance Imaging system (MRI): with the ability to produce large magnetic fields, it has been used for a long time helping in the detection of a substantial number of medical conditions. It is thought that with some modifications this system can be used to accurate control microrobots for clinical use as well as provide a good localization method [26,27].

LOCALIZATION

Localizing and tracking microrobots bring problems that are a bit easier to solve than locomotion problems because of the fact that imaging systems for medical use have been around for a long time, hence many methods for localizing specific objects and other types of foreign materials have already been developed. They range from electromagnetic to ultrasound-based methods, fluoroscopy, computed tomography, infrared and emitted radiation, and also MRI localization methods. Nevertheless, there are still important factors in determining microrobots' position inside the human body such as the spatial resolution and acquisition rate of images [3].

Electromagnetic and magnetic localization methods are achieved by the presence of trackers in the device that cause voltage spike detection and magnetic field variation detection [28,29]. Using radiation markers, tracking microrobots is also possible: with fluoroscopy techniques giving us high-resolution 2D images and with Computed Tomography scans (CT scans) that offer good, low-contrast resolution images which are later capable of producing a 3D image [30,31]. MRI already provides good imaging method for determining various medical conditions and can also be used to track groups of nanoparticles, though depending on the material used in the microrobot, some ferromagnetic objects may cause image artifacts [32]. Ultrasound tracking methods are the only ones to combine good resolution, minimal adverse health effects, high speed, safety, adequate frame rates, and low-cost prices for localization in soft

tissue. Also, combined with MRI assistance, it can even overcome some of its disadvantages like low Signal to Noise Ratio (SNR) [33].

IMPACT/APPLICATIONS

Current minimal invasive methods and techniques reduce postoperative patient recovery, less pain, less infection risks, overall cost, and consequently increasing healthcare quality [3,34]. Furthermore, microrobots have a lot of potential to continue improving on these goals, especially for contactless biomedical applications from:

- targeted therapy, in the delivery of radiation for cancer treatment, or other chemical and biologic component; and perform thermoablation of specific areas without damaging healthy body parts [35,36].
- biopsies, for ablation and tissue removal from difficult-to-reach areas [2].
- structural components, to serve as simple scaffolds or stents or even as tiny implants and special electrodes for use in brain and muscle tissue stimulation [3,37].
- and telemetry, transmitting signals for remote sensing and localization [3].

And in several medical areas such as:

- cardiology, microrobots can easily navigate through all the blood vessels and reach desired location goals and also removing clots, or act as stents [20,38].
- neurology, microrobots can also navigate natural pathways inside the brain and spine, and heavily impact cancer treatments for the central nervous system [39,40].
- and urology, the urinary system is also composed of natural pathways from microrobots to reach certain areas in order to treat kidney stones or offer minimally invasive access to the prostate for cancer treatments [41,42,43].
- obstetrics, pregnancy complications often require open surgery to prevent death, malformations, or impairments on growing fetuses and these kinds of surgeries are quite difficult given to the risks taken. Specially designed microrobots can perform occlusions in tracheal and urethra systems or even perform ablation of some malformations [44,45].
- ophthalmology, for retinal microsurgeries [46,47]. and otolaryngology, for delivering stem cells in the inner ear, and reduce trauma and infection in cochlear implants [48,49].

1.2 STATE OF THE ART

In this state of the art, several work studies will be presented regarding existing projects and designs of microrobots that are able to swim in a low- Re fluids and simultaneously carry a load to be delivered at a specific site, at least ideally. Additionally, it will be addressed some of the current methods used to calculate the intrinsic property of sperm flagella: the bending stiffness.

MICROROBOTS DESIGNS

Microrobotics has been around for a few years now and so are the concepts already designed for applications in minimal invasive interventions [3]. Despite the significant number of designs that are purely artificial, the study will only present recent concepts of biohybrid microrobots capable of swimming in low- Re fluids and drug transport capacity since they are the most similar to the microrobot presented in this work.

All the following concepts have a biohybrid approach combining existing biological structures with a manmade functional components:

Gao *et al.* (2013) designed a plant-based bioinspired magnetically propelled helical microswimmer [50]. Inspired by spiral plant water-conducting vessels, thin layers of titanium and nickel (Ti-Ni) are sequentially deposited on these structures followed by the removal of the organic material results in a simple and cost-effective mass production process of functional helical microswimmers. These propellers show efficient propulsion results in biological media like human serum, reaching speeds over $250 \mu\text{m} \cdot \text{s}^{-1}$.

Williams *et al.* (2014) were the first to develop a microrobot capable of swimming in low- Re with a unique fabrication process [51]. They developed a swimmer made of a polydimethylsiloxane filament with a short and ridged head, and a long and thin tail on which cardiomyocytes are cultured. These cardiac cells are the ones responsible for propelling the swimmer, by contracting and deforming the filament. These biohybrid swimmers can achieve speeds of 5 to $10 \mu\text{m} \cdot \text{s}^{-1}$, and when creating a 2-tail swimmer it is possible to reach $81 \mu\text{m} \cdot \text{s}^{-1}$.

Sahari *et al.* (2014) thought of combining non-pathogenic bacteria with artificial particles to achieve targeted delivery of therapeutic agents [52]. They assembled

motile *Escherichia coli* MG1655 bacteria together with elliptical disk-shaped carboxylate polystyrene microparticles to create what they called BacteriaBots. These BacteriaBots achieve transportation by chemotaxis. In other words, by providing a steady linear concentration gradient of a chemoattractant they proved possible, in their study, that these bacteria were capable of extravascular transport in response of chemotactic stimuli.

Zhuang *et al.* (2015) studied the ability of some flagellated bacteria to navigate through a medium in response to pH gradients [53]. They demonstrated that microrobots based on these bacteria can exhibit unidirectional and bidirectional pH-tactic behaviours under 3 configured pH gradients. Consequently, these biohybrid microsystems could be applied to sense cancerous cells that induce these types of gradients in stagnant fluids inside the human body and also perform TDD. Swimming speed of these pH gradient driven microrobots are highly influenced by other factors such as heat and chemical concentrations, but it's possible to achieve speeds up to $10 \mu\text{m} \cdot \text{s}^{-1}$.

Srivastava *et al.* (2015) devised a microsystem able to perform cellular surgery with drug rehabilitation [54]. Calcified porous microneedles with a length of 40 to 60 μm were extracted from *Dracaena* plant species and posteriorly coated with a magnetic iron-titanium (Fe-Ti) layer for posterior external actuation. By applying a rotating magnetic field, the microneedles achieve a drilling function caused by the shifting from rotating parallel to the substrate to vertical position. Once inside the cell, drugs such as chemotherapy can be delivered precisely into tumour cells.

Felfoul *et al.* (2016) proved possible for magnetotactic bacteria to be manipulated in order to reach areas of tumour regions that are currently difficult to access [55]. Using a *Magnetococcus marinus* strain, MC-1, that naturally contain chains of iron-oxide nanocrystals, they showed possible to use external magnetic actuation to penetrate oxygen-depleted hypoxic regions of tumours. Once there, the nanoliposomes containing drugs for targeted therapy that are bound covalently to MC-1 cells can interact with cancer cells, effectively treatment.

Khalil *et al.* (2016) made robotic sperm cells fabricated from polystyrene and iron-oxide particles that enabled magnetic actuation of the microswimmer [56]. They proposed a robotic system that has similar swimming behaviour and morphology to

those of live sperm cells. The swimming speed of these robotic sperms can be up to $125 \mu\text{m} \cdot \text{s}^{-1}$, which is relatively faster than others in low- Re conditions.

Xu *et al.* (2017) developed a sperm-driven micromotor for targeted drug delivery in female reproductive systems [57]. A magnetic tetrapod microstructure was designed so that it can mechanically trap the heads of sperm cells and transport an anticancer drug to be delivered in tumour walls and spheroids, ultimately achieving a propeller system actuated by external magnetic fields capable of swimming low- Re environments.

Yasa *et al.* (2018) created a biohybrid microrobot by combining unicellular *Chlamydomonas reinhardtii* alga and polyelectrolyte-functionalized magnetic $1 \mu\text{m}$ spherical cargoes that are attached to the biologic surface via noncovalent interactions [58]. These algal microswimmers were proved to be cytocompatible when co-cultured with healthy and tumorous cells. Furthermore, the spherical cargoes enable external magnetic actuation for propulsion in living bodies, making this microswimmer with great biocompatibility highly suitable for targeted drug delivery therapies

Sun *et al.* (2019) proposed a pine pollen-based micromotor (PPBM) microrobot capable of cargo transportation to achieve controlled drug release [59]. These PPBM are created by the encapsulation of magnetic particles Fe_3O_4 and medicine into hollow air sacs of pine pollen, via vacuum loading achieving great structure uniformity, morphological stability, and biocompatibility. Swarm propulsion in biological fluids by actuation of external magnetic fields is also possible enabling controllable drug carriers.

All these presented studies showed successful progress in creating and designing microrobotic systems that are capable of performing some kind of minimal surgical intervention without major damage to organs and tissues. Additionally, they can all be localized to some extent with non-invasive methods like ultrasound. Despite the achievements of these authors' works, there is still a lack of knowledge regarding microrobots ideal locomotion strategies in the difficult low- Re environment as well as an efficient localization mechanism capable of getting good images at this scale.

Magdanz *et al.* (2019) developed a biohybrid soft microrobot that has achieved forward propulsion in low- Re fluids by applying rotating magnetic fields called IRONSperm [25]. They are made by electrostatic self-assembly of magnetic particles

with dead bull sperm cells resulting in a magnetic coat of the sperm's head and flagella. They found that IRONSperm can achieve swimming speeds of $6 \text{ to } 8 \pm 4.1 \mu\text{m} \cdot \text{s}^{-1}$ at an actuation frequency of 8 Hz and 45° precision angle. Biocompatibility and drug loading ability were also tested and successfully verified. Moreover, the magnetic coat of the microswimmer increases the acoustic impedance of the cell which made possible for ultrasound feedback localization.

This last microrobot design is also the one that most resembles the ones used during this work since its only dissimilarity is on the particles used in its fabrication process. Despite their differences, they face the same limitations as the additional magnetic coating influences intrinsic properties of the spermatozoa's tail. As previously stated, these intrinsic properties are very important in determining its propulsive thrust that is characterized by its Sperm number (Sp), hence the importance of further studies.

BENDING STIFFNESS DETERMINATION MECHANISMS

Elastic forces play an important role when it comes to navigate through hard conditions such as the ones found in viscous mediums [15]. Despite such difficulties, a lot of organisms found the perfect way to overcome it, and although many remain unknown, the following studies were able to make determinations related to how some organic life structures allow microorganisms to achieve propulsion thrust in low- Re fluids, namely the bending stiffness and/or similar resistive elastic forces:

Lindemann *et al.* (1973) determined the elastic rigidity (stiffness) of impaled motionless bull sperm flagella by manipulating its tail with a probe technique in relation to external concentration of ATP (adenosine triphosphate) and ADP (adenosine diphosphate) [60]. The method worked by stationing a sperm cell stretched along the x-axis and using a microprobe tip to push the tail, its position is changed followed by the calculation of the time it takes to the cell's flagella return to its original position. This is a relaxation method that is also used in this project, but it will be explained in further detail in the next chapter. They demonstrated that in a concentration of 10 mM ATP medium the average measured stiffness is $4.0 \times 10^{-21} \text{ N} \cdot \text{m}^2$ and that is also highly dependent on the medium concentration of ATP in contrast with zero correlation between ADP and bending stiffness of the flagella.

Harada *et al.* (2007) measured the Young's modulus of cilia found in renal tubular epithelial cells using optical tweezers [61]. Polystyrene microspheres were placed on

the tips of the cilia so that it could be exerted minute forces by an infrared Nd-YAG laser beam apparatus optically traps the microspheres. By then measuring the microsphere's displacement, the Young's modulus was examined and depending on the length of the cilia, in μm , it ranges from 0.5 to $6 \times 10^{-15} N.m^2$.

Hill *et al.* (2010) used magnetic beads to examine the force produced by motile cilia against an external load and estimated its stiffness [62]. Using pole tips to exert forces towards cilia from human bronchial epithelial cells they found that this external influence caused reduction in axoneme beat amplitude, reduction in tip velocity proportionate to applied forces and no significant changes in beat frequency. Consequently, they proved that the direction of the force applied does not influence the estimated bending stiffness.

Xu *et al.* (2016) studied the flexural rigidity and shear stiffness of cilia using bends and counterbends [63]. After the fixation of unicellular alga *Chlamydomonas reinhardtii*, optical tweezers exerted bends and counterbends on the tips of motile cilia from the organism and determined that the average intrinsic flexural rigidity is $0.84 \pm 0.28 \times 10^{-21} N.m^2$ and the elastic resistance to interdoublet sliding, shear stiffness, has a value of $0.79 \pm 0.11 \times 10^{-22} N.m^2$.

This last study proved that important details regarding elasto-hydrodynamic interactions and highly efficient wave propagation of sperm cells are still not fully comprehended due to lack of characterization of mechanical properties like the internal resistive forces of the flagella. Additionally, all the previous studies focused on determining some intrinsic properties of live sperm cells and similar structures making direct contact with them, hence adding external influence on the calculated properties. Furthermore, along with the varying bending stiffness of the sperm tail and its magnetic coating, the rotation frequency at which the microrobots are actuated is also something that needs further research, since it is the main characteristic that will determine the swimming speed of the microrobot as long as an important parameter in the equation for the Sperm number.

1.3 MOTIVATION

Hydrodynamic interactions in low- Re are ruled by the rheological properties of the viscous medium the elastic properties of the swimmer, and the frequency of beating tail deformations. These conditions define the pattern of the transverse waves that propagate along the soft body, namely the mean flagellar curvature of the flagellar beat. This is directly proportional to the curvature of the swimming path of the cell, which is essential to provide maximum propulsive thrust, along with a proper bending stiffness unit [64].

The motion characteristics of a magnetically actuated passive flagellum differs from that of a living cell in that passively propagating waves initiated from a boundary cannot resemble those observed on an active flagellum with distributed contractile elements [65]. Adding to that, cellular segments of the magnetically actuated passive flagellum are randomly coated with nanoparticles, leading to notably different mechanical properties from that of active flagella. In other words, during fabrication, the location of the attachment site of the nanoparticles varies from cell to cell due to random electric charges in the membrane surface of spermatozoa resulting in different magnetized cellular segments along the flagellum. Furthermore, the bending stiffness along the length of the flagellum is an important parameter to enable correct theoretical predictions and simulations of sperm motion. Thus, giving the varying shape of sperm cells tail, the importance of the location of the magnetic segment along the flexible filament was proposed [66].

In practice, measuring the exact bending stiffness of flagella is difficult in terms of implementation because it relies on excitation of a soft organic body at the microscale and relating a measurable response to desirable mechanical properties. Most of the studies mentioned previously focused on live sperm cells, and despite the importance of these approaches in the determination of the bending stiffness, the properties of passive flagella and active flagella must still be investigated.

Here, it is considered the impact of additional functionalities on the flagellum's bending stiffness, such as magnetization and surface coating. Sperm-templated, self-assembled microrobots comprise a heterogeneity in terms of the particle distribution along their tail that is particularly useful when designing and optimizing flexible swimming microrobots.

In this work, the spatially varying bending stiffness due to the nonuniform magnetic nanoparticle coating along sperm flagella is characterized. The motivation behind this project is that given the lack of this crucial knowledge in the microrobotics' field, further research into looking for the perfect microswimmer is needed so that they can perform the desired tasks mentioned in previous sections.

OBJECTIVES

To achieve such goals there are several objectives to be fulfilled in this work:

- first, an intense research of the microrobotics world, how it works and what laws is governed by is conducted. As this theme was never taught in any previous courses, a careful and detailed study must be made so that the tasks that follow are easily accomplished. Additionally, magnetic methods for robotic applications must also be studied to fully comprehend the actuation systems that are going to be used;
- then, after reasonable understanding off the subject, calculate the bending stiffness of a coated sperm cell using the electromagnetic system provided;
- next, is to look for the various configuration of SPINOSperms and conduct the experiment protocol on them;
- investigate possible microstructures for construction a control group that can confirm magnetic actuation of magnetic flagella;
- and finally, study possible correlations between theoretical and data results and categorize them in proper groups.

CHAPTER 2 – MATERIALS AND METHODS

The materials and methods used in this work will be presented in this chapter. First, a detailed description of the fabrication process of the biohybrid soft microrobots followed by the methods and calculations used for obtaining simulation results on the varying bending stiffness as well as the actual results from the experiments on the samples.

2.1 MICROSWIMMER FABRICATION

IRONSpems are fabricated by using a suspension of rice grain-shaped maghemite nanoparticles ($\gamma\text{Fe}_2\text{O}_3$) roughly 100 nm diameter size and bovine sperm cells with a 60 μm length. The particles are combined with the cells through electrostatic forces, namely, van der Waals and Coulombs forces [24]. These particles also display an average surface zeta potential of 12.9 mV in water whereas normal sperm cells have an overall net negative surface potential with nonuniform distribution of charges also allowing the existence of some areas with neutral and positive charges that determine the amount of particles that will coat the flagella [67].

For the experiments conducted, a different kind of IRONSperm was used called SPINOSperm. The fabrication process of these SPINOSperms is essentially the same only differing on the magnetizable nanoparticles used in its production: spinel particles of AB_2X_4 formula, in this study case, the nanoparticles used are CoFe_2O_4 [68].

These spinel particles are used instead of maghemite nanoparticles when mixing them with a sperm solution. A primitive bull sperm solution goes through a washing process: 5 minutes centrifugation at 300g and after that, the supernatant is removed and resuspended in water and only then nanoparticles are added. The result is a solution containing dead bovine sperm cells coated with these magnetic nanoparticles that are aggregated along the flagella, ultimately creating a bio-hybrid microrobot: the sperm cell provides structure and means of propulsion in low- Re and the nanoparticles allow the external magnetic actuation.

Sperm cells reveal a non-uniform distribution charge distribution along the flagella which consequently allows different nanoparticle aggregation sites providing segments that can be individually magnetized culminating in a total of 15 different configurations of SPINOSperm. These bovine spermatozoa display 4 morphological distinct areas: head, midpiece, principal piece, and distal piece (h, m, p, d).

Considering that the head of the microrobots always sticks to the bottom of the lamella glass, providing an anchor spot for the fixation of the microswimmer, whether it is coated or uncoated, the 15 original configurations fall to 7 possible configurations that can be seen in Figure 4: for representational purposes, if the midpiece is coated $m = 1$, if the principal piece is coated $p = 1$, if the distal piece is coated $d = 1$, and if a flagellar segment is uncoated $m = 0, p = 0, d = 0$.

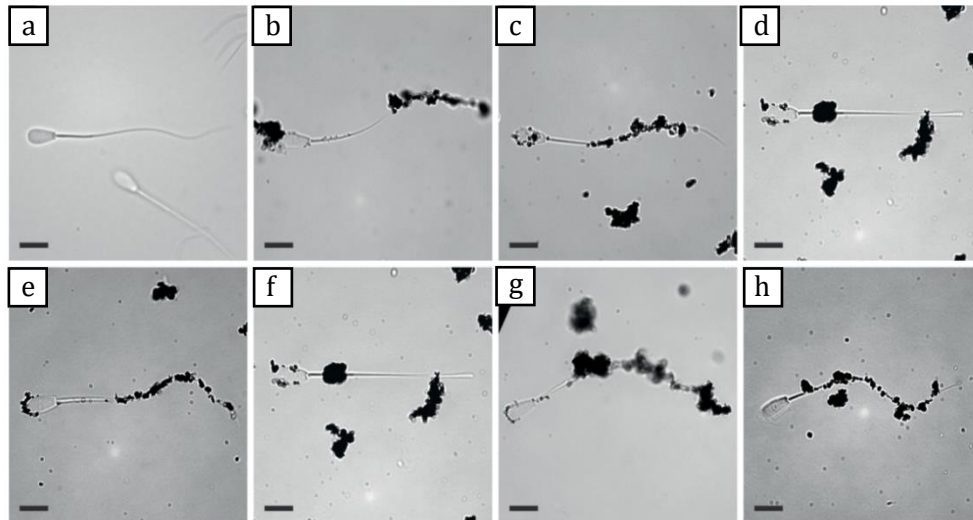


FIGURE 4 Microscopic images of dead bovine sperm cells coated with maghemite nanoparticles with different assembly sites. (a) normal sperm cell. (b) distal piece coated. (c) principal piece coated. (d) midpiece coated. (e) principal and distal pieces coated. (f) midpiece and distal piece coated. (g) midpiece and principal piece coated. (h) fully coated. Adapted from Magdanz *et al.* (2021) [69].

2.2 BENDING STIFFNESS ESTIMATION

NANOPARTICLE COATED SOFT FLAGELLUM

It was mentioned in the previous chapter that an effective means of navigation through various fluidic mediums is traveling-wave propulsion. If a deformation wave begins at the proximal end of the flagellum propagating towards its distal end, the steady-state solution of the balance of forces acting on any segment along the uniform filament will depend only on the sperm number [15, 64]. Recalling Equation (4), $Sp = l(|\omega|\xi_{\perp}/\kappa)^{1/4}$, $\kappa = IE$, is only true if the material has uniform elastic modulus, E , and uniform moment of cross-section area, I , along the length of the flagellum.

As shown before, the sperm cells' tail has a unique morphologic shape due to its complex internal structure consisting of centre and outer microtubules, gradually

tapering towards the distal end as depicted in Figure 5(a). Therefore, the normal drag coefficient, ξ_{\perp} , varies along the length as:

$$\xi_{\perp}(x) = \frac{4\pi\eta}{\log\left(\frac{l}{D(x)}\right) - 1} \quad (5)$$

where η is the viscosity of the fluid, and $D(x)$ is the varying diameter of the flagellum along x .

Due to the location and concentration of nanoparticles on coated sperm cells, the elastic modulus of the flagellum will also vary along the length based on the rule of mixture such that:

$$E(m, p, d; x) = \begin{cases} E_s + \phi(E_p - E_s)m, & x \in \mathcal{L}_m \\ E_s + \phi(E_p - E_s)p, & x \in \mathcal{L}_p \\ E_s + \phi(E_p - E_s)d, & x \in \mathcal{L}_d \end{cases} \quad (6)$$

where E_s is the modulus of elasticity of the organic body, E_p is the modulus of elasticity of the nanoparticles, and ϕ is the volume fraction between the organic body and the nanoparticles. Also, $\mathcal{L}_m = \{0 \leq x \leq l_m\}$, $\mathcal{L}_p = \{l_m \leq x \leq l_m + l_p\}$ and $\mathcal{L}_d = \{l_m + l_p \leq x \leq l\}$, where l_m is the length of the midpiece and l_p is the length of the principal piece.

Similarly, it is also possible to determine the influence of the particle coating on the moment of area of the flagellum based on the volume fraction ϕ . If V_s and V_p represent the volumes of the organic body and the nanoparticles respectively, the volume fraction is $\phi = V_p/(V_p + V_s)$ and it varies across the soft filament as follows:

$$\phi(m, p, d; x) = \begin{cases} m\phi, & x \in \mathcal{L}_m \\ p\phi, & x \in \mathcal{L}_p \\ d\phi, & x \in \mathcal{L}_d \end{cases} \quad (7)$$

Furthermore, the diameter of the flagellum also varies along the length influence the moment of area I . To count for this implication, let us consider a segment of length Δx that has a volume of $\Delta V_s = \pi d_f^2 \Delta x / 4$, where d_f is the diameter of the coated sperm cell along the flagellum. The volume of the nanoparticle coated segment is then $\Delta V = \pi d_f^2 \Delta x / (4(1 - \phi))$. Consequently, the diameter of the coated flagellum scales with the diameter of the uncoated flagellum as $\sim (1 - \phi)^{-0.5} d_f$ and we get:

$$D(m, p, d; x) = \begin{cases} (1 - m\phi)^{-0.5} d_f, & x \in \mathcal{L}_m \\ (1 - p\phi)^{-0.5} d_f \left(1 - f \frac{x - l_m}{l_m + l_d}\right), & x \in \mathcal{L}_p \\ (1 - d\phi)^{-0.5} d_f \left(1 - f \frac{x - l_m}{l_m + l_d}\right), & x \in \mathcal{L}_d \end{cases} \quad (8)$$

where $f = (l_p + l_d)/L$ is the taper factor of the flagellum. The moment of area of the filament is then:

$$I(m, p, d; x) = \frac{\pi}{4} \left(\frac{D(m, p, d; x)}{2} \right)^4 \quad (9)$$

Thus, for any actuation frequency ω , the nanoparticle coated flagellum of the microswimmer will have a bending stiffness κ and sperm number Sp that are influenced by the volume fraction $\phi(x)$, when a dynamic magnetic field is applied.

MAGNETIZED CELLULAR SEGMENTS IN A MAGNETIC FIELD

The nanoparticles also have an effect on the dynamic response of the tail when an external magnetic field \mathbf{B} is applied. The magnetic field magnetizes the clusters of nanoparticles to a magnetization $\mathbf{m}(m, p, d; x)$ that is directly proportional to the distribution of bending moment $\mathcal{B}(m, p, d; x)$, yielding $\mathcal{B}(m, p, d; x) = V_p \|\mathbf{m}(m, p, d; x) \times \mathbf{B}\|$.

Including the influence of the volume fraction in the distribution of bending moment:

$$\mathcal{B}(m, p, d; x) = \begin{cases} \frac{\pi m \phi \Delta x \|\mathbf{m}\| \|\mathbf{B}\|}{4(1 - m\phi)} d_f^2, & x \in \mathcal{L}_m \\ \frac{\pi p \phi \Delta x \|\mathbf{m}\| \|\mathbf{B}\|}{4(1 - p\phi)} d_f^2 \left(1 - f \frac{x - l_m}{l_m + l_d}\right)^2, & x \in \mathcal{L}_p \\ \frac{\pi d \phi \Delta x \|\mathbf{m}\| \|\mathbf{B}\|}{4(1 - d\phi)} d_f^2 \left(1 - f \frac{x - l_m}{l_m + l_d}\right)^2, & x \in \mathcal{L}_d \end{cases} \quad (10)$$

The distribution of bending moment includes a maximum magnetic torque exerted $V_p \|\mathbf{m}(m, p, d; x)\| \|\mathbf{B}\|$, which implies that the flagellum will undergo maximum deformation.

RELAXATION METHOD

The small deformation will be governed by an equilibrium of the elastic and magnetic forces, F_{el} , and the drag force of the fluid, F_{visc} :

$$F_{el} + F_{visc} = 0 \quad (11)$$

where the elastic and magnetic force is:

$$F_{el} = \frac{\partial^2 \mathcal{B}(m, p, d; x)}{\partial^2 x} + \frac{\partial^2}{\partial x^2} \left(\kappa(m, p, d; x) \frac{\partial^2 y}{\partial x^2} \right) \quad (12)$$

and the viscous force is given by:

$$F_{visc} = -\xi_{\perp}(x) \frac{\partial y(x, t)}{\partial t} \quad (13)$$

where $y(x, t)$ is the small amplitude of deviation from the equilibrium position and can be measured with respect to the sample frame of reference of the sperm head (e_1, e_2) as shown in Figure 5(c).

In the case where the head is fixed to a solid boundary, both the amplitude $y(0, t)$ and its derivative, $y(0, t)/\partial x$, are zero. Once an external magnetic field, \mathbf{B} , is applied, the nanoparticles become magnetized, and the distribution of bending moment is introduced. The total magnetic torque exerted on the magnetic dipole moment of the

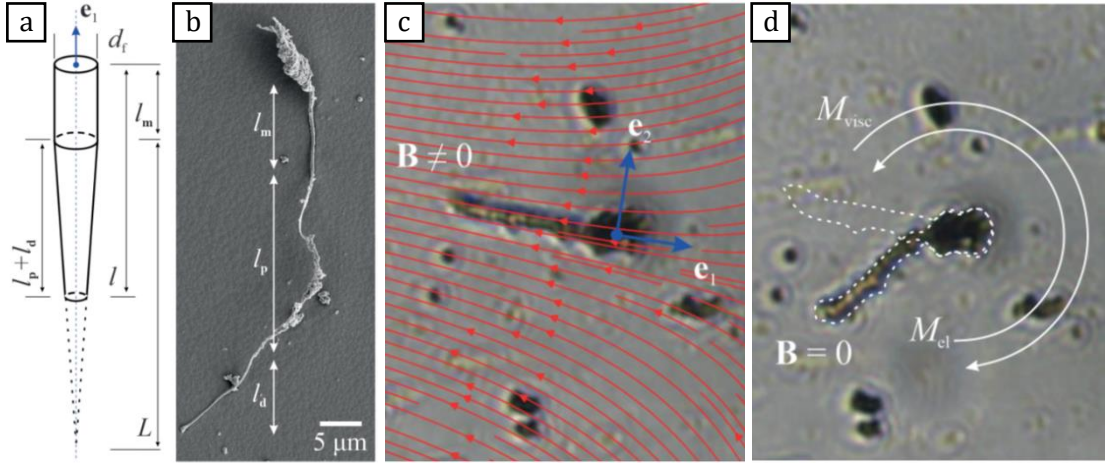


FIGURE 5 The bending stiffness varies along the flagellum due to a change in moment of area, $I(m, p, d, x)$, and elastic modulus, $E(m, p, d, x)$. (a) It tapers gradually toward the distal end with a taper factor f . (b) The location of the magnetizable cellular segment is determined during electrostatic self-assembly and the indices m, p, d designate the magnetized region. (c) The applied field, B , produces elastic deformation of the flagellum using magnetic torque exerted on its dipole moment. (d) The elastic bending resistance of the passive flagellum is balanced by the viscous drag in the surrounding fluid when the applied field is removed, $B = 0$. Adapted from Magdanz *et al.* (2021) [69].

flagellum produces a deformation on the axis $e_1 \times e_2$. Thus, for a given distribution of nanoparticle coating along the flagellum, its excitation and deformation can be predicted.

It is also possible to determine the relaxation of the deformation with the relation from Equation (12), which depends on the varying bending stiffness along the length of the flagellum. Assuming that the taper factor is relatively small, $f \approx 0$, and that the bending stiffness is segment-wise constant, and by the rule of mixture:

$$\kappa(m, p, d; x) = \begin{cases} \kappa_m, & x \in \mathcal{L}_m \\ \kappa_p, & x \in \mathcal{L}_p \\ \kappa_d, & x \in \mathcal{L}_d \end{cases} \quad (14)$$

Assuming as well that the decay time of all the magnetizable segments is the same, the solution of the force balance is as follows:

$$y(x, t) = w(m, p, d; x) e^{-\frac{t}{\tau(m, p, d)}} \quad (15)$$

where $w(m, p, d; x)$ is the position dependent mode shape function and $\tau(m, p, d)$ is the decay time of the flagellum to its original configuration.

Similarly, the mode shape of each cellular segment is written as:

$$w(m, p, d; x) = \begin{cases} w_m, & x \in \mathcal{L}_m \\ w_p, & x \in \mathcal{L}_p \\ w_d, & x \in \mathcal{L}_d \end{cases} \quad (16)$$

Substituting Equation (15) for segment-wise constant bending stiffness into Equation (11) yields:

$$\kappa(m, p, d; x) \frac{d^4 w(m, p, d; x)}{dx^4} = \frac{\xi_{\perp}}{\tau(m, p, d)} w(m, p, d; x) \quad (17)$$

The general solution for the mode shape of the midpiece is:

$$\begin{aligned} w_m(m, p, d; x) = & A_{1m}(m, p, d) e^{r_m(m, p, d)x} + \\ & A_{2m}(m, p, d) e^{-r_m(m, p, d)x} + A_{3m} \sin(r_m(m, p, d)x) \\ & + A_{4m}(m, p, d) \cos(r_m(m, p, d)x) \end{aligned} \quad (18)$$

The general solution for the mode shape of the principal piece is:

$$\begin{aligned} w_p(m, p, d; x) = & A_{1p}(m, p, d) e^{r_p(m, p, d)x} + \\ & A_{2p}(m, p, d) e^{-r_p(m, p, d)x} + A_{3p} \sin(r_p(m, p, d)x) \\ & + A_{4p}(m, p, d) \cos(r_p(m, p, d)x) \end{aligned} \quad (19)$$

The general solution for the mode shape of the distal piece is:

$$\begin{aligned} w_d(m, p, d; x) = & A_{1d}(m, p, d) e^{r_d(m, p, d)x} + \\ & A_{2d}(m, p, d) e^{-r_d(m, p, d)x} + A_{3d} \sin(r_d(m, p, d)x) \\ & + A_{4d}(m, p, d) \cos(r_d(m, p, d)x) \end{aligned} \quad (20)$$

where $A_{im}(m, p, d)$, $A_{ip}(m, p, d)$, and $A_{id}(m, p, d)$ are the i th constant depending in the conditions at the midpiece, principal piece and distal piece, respectively, for $i = 1, \dots, 4$.

Integrating the mode shape of Equation (16) in Equation (17) yields:

$$\tau(m, p, d) = \frac{\xi_{\perp}(m, p, d)}{r_m^4(m, p, d)\kappa_m} = \frac{\xi_{\perp}(m, p, d)}{r_p^4(m, p, d)\kappa_p} = \frac{\xi_{\perp}(m, p, d)}{r_d^4(m, p, d)\kappa_d} \quad (21)$$

Finally, applying the boundary conditions for the ends of the flagellum:

$$w(m, p, d; 0) = \frac{dw(m, p, d; 0)}{dx} = 0 \quad (22)$$

$$\frac{d^2 w(m, p, d; l)}{dx^2} = \frac{d^3 w(m, p, d; l)}{dx^3} = 0 \quad (23)$$

Since the connection between the three pieces is continuous and smooth, it yields:

$$\frac{d^i w_m(m, p, d; l_m)}{dx^i} = \frac{d^i w_p(m, p, d; l_m)}{dx^i} \quad (24)$$

$$\begin{aligned} & \text{for } i = 0, \dots, 3. \\ \frac{d^i \omega_p(m, p, d; l_m + l_p)}{dx^i} &= \frac{d^i \omega_d(m, p, d; l_m + l_p)}{dx^i} \\ & \text{for } i = 0, \dots, 3. \end{aligned} \quad (25)$$

Using all the previous boundary conditions, the following system of algebraic homogenous equations is obtained:

$$\mathcal{M}(r_m(m, p, d))\mathcal{A} = 0 \quad (26)$$

where \mathcal{M} is a coefficient matrix and \mathcal{A} is a vector with the mode shape constants $A_{im}(m, p, d)$, $A_{ip}(m, p, d)$, and $A_{id}(m, p, d)$, from Equations (18)–(20). The matrix \mathcal{M} is characterized by one of the constants $r_m(m, p, d)$, $r_p(m, p, d)$, or $r_d(m, p, d)$. Since they are related based on the decay time $\tau(m, p, d)$ from Equation (21).

The aim with these previous equations and relations is to obtain the bending stiffness for each of the seven groups of nanoparticle-coated sperm cells, given a set of parameters without simulating the dynamic response to determine the relaxation time.

Additionally, the relation between bending stiffness κ and decay time τ for homogenous tails can be extended and used based on numerical and experimental results [69].

For groups with non-homogeneous bending stiffness, with κ depending on x , it is defined an apparent bending stiffness as:

$$\langle \kappa(m, p, d) \rangle = \left(\frac{l}{\mu} \right)^4 \frac{\xi_{\perp}}{\tau(m, p, d)} \quad (27)$$

where $\mu = 1.875$ is the first mode of the characteristic force balance Equation (11) when the magnetic field is removed, the operator $\langle \kappa(m, p, d) \rangle$ is the average bending stiffness over the length of the flagellum, l , and $\tau(m, p, d)$ is the decay time to the initial configuration.

This extended definition gives the same results for homogenous groups and by solving Equation (11), given a certain set of parameters (ϕ , E_s , and E_p), a direct determination of the bending stiffness can be made from the calculated or measured dynamic response of the flagellum after the removal of the magnetic field.

Combining Equation (21) with Equation (27), the apparent bending stiffness can be calculated as follows:

$$\langle \kappa(m, p, d) \rangle = \left(\frac{r_m(m, p, d)l}{\mu} \right)^4 \kappa_m \quad (28)$$

Then, determining the bending stiffness based on the constant $r_m(m, p, d)$ is very simple through the simulation results.

2.3 EXPERIMENTAL SETUP

To produce an external magnetic field capable of exerting the type of magnetization mentioned before, two orthogonal electromagnetic coils with a tilt angle of 70° with respect to the horizontal x-y plane, and another tilt angle of 70° with respect to the vertical x-z plane, spaced from each other 10 cm were used. Each electromagnetic coil has 3200 turns with a 0.7 mm copper wire thickness resulting in hollow cylinders with 20 mm inner diameter, 40 mm outer diameter, and a length of 80 mm.

As shown in Figure 6(c)(e), the electromagnetic coils are placed over two 3D printed acrylic structures that hold the coils at the angles mentioned, as well as integrating them on the Zeiss Axio Vert.A1¹ microscope stage, leaving enough space for sample slides to be put in place.

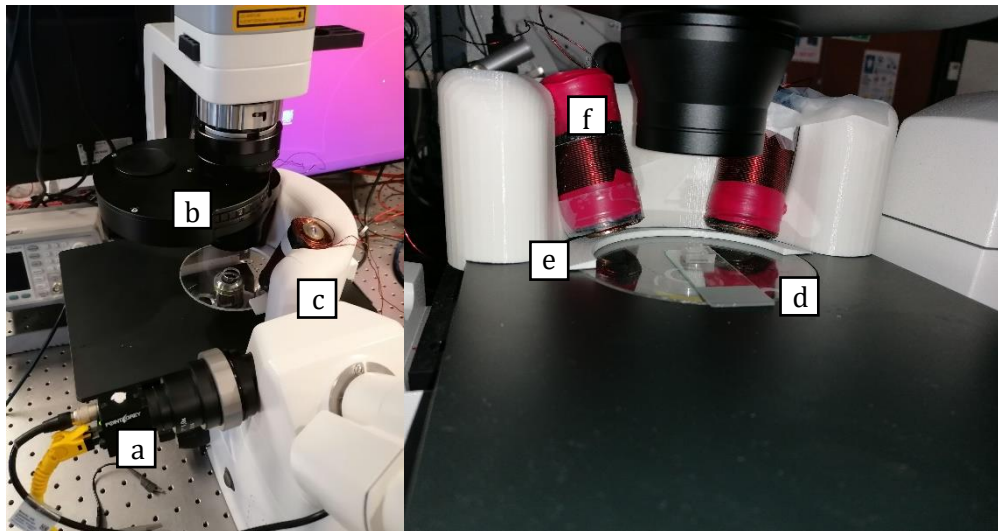


FIGURE 6 Experimental setup illustration. (a) camera. (b) image filter. (c) 3D-printed coil holder. (d) Plexiglas disk do hold sample laminas. (e) supporting semi-circular wedge. (f) electromagnetic coil.

The experimental set up comes with a software platform that enables the user to set all the parameters needed to conduct the experiments, such as magnetic field strength, frequency of excitation, and direction of excitation. Thus, resulting in a mechanism capable of actuating the nanoparticles attached to sperm cell's tail at a certain direction and frequency of rotation, as well as powering on and off the exerted magnetic field. This system was designed in SolidWorks software at the Surgical Robotics Laboratory (SRL) from the Department of Biomechanical Engineering at University of Twente.

¹ www.zeiss.com/microscopy/int/products/light-microscopes/axio-vert-a1-for-biology

To have a more comprehensive understanding of the magnetic field's behaviour, a simulation of the exerted magnetic fields can be found below in Figure 7.

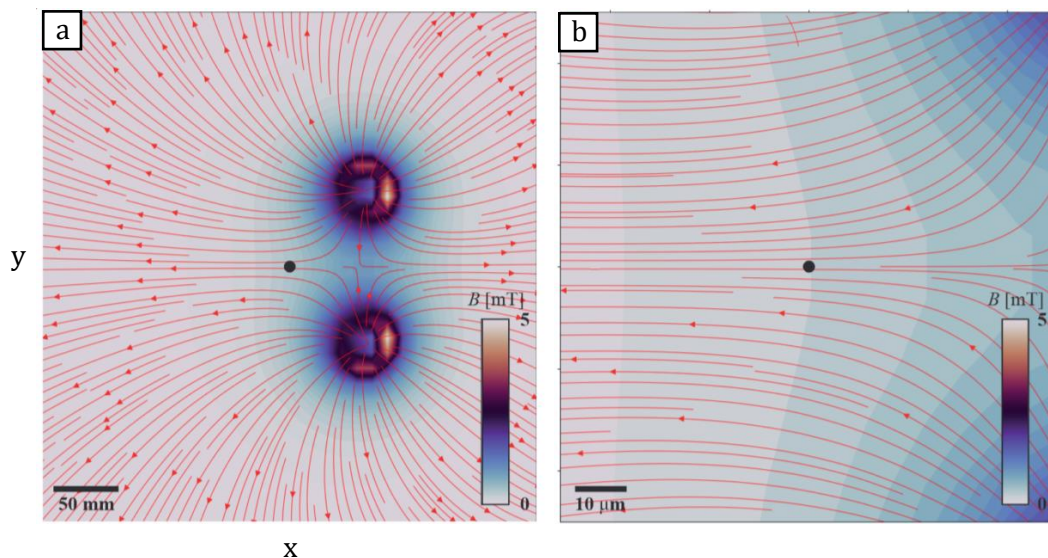


FIGURE 7 Representation of the applied external magnetic field. (a) The magnetic fields of each coil are superimposed and controlled to dynamically excite the flagellum. (b) Field strength of 5 mT is applied at the position of the flagellum marked as the black dot. Adapted from Magdanz *et al.* (2021) [69].

The samples were prepared so that precipitation of the cells occurs on a horizontal slide as the head of the sperm cell adheres to the surface, leaving the tail free in the water in order to be excited by a superimposed magnetic field with a maximum superimposed intensity of 5 mT, which consequently leads to the elastic deformation of the flagellum. Then, the relaxation of the tail is obtained when the magnetic field is turned off so that the tail can return to the original position.

The dynamic excitation and relaxation of the samples are then repeated several times and recorded with a with a 2.3 megapixels CMOS Axiocam 702 mono² camera from Carl Zeiss B.V., Oberkochen, Germany. Data extraction is then possible through MATLAB scripts developed by the SRL, with some later modifications to allow the raw videos to be cropped in desirable sizes in order to simplify the calculation of the bending stiffness of the experimented sample. This process will be further explained later in the next chapter.

² www.zeiss.com/microscopy/int/products/microscope-cameras/axiocam-702-mono

2.4 CONTROL GROUP

One other important step in this work was to validate the magnetic excitation method used, so it was idealized the creation of a structure with known bending stiffness to serve as control group for testing the ability of the electromagnetic-coil system provided.

First, a two-photon lithography (2PL) system was used to create 3D designs of cantilevers and similar structures with identical form and physical properties of the microrobots studied [71]. The 2PL system used was a commercial negative-tone, acrylate-based photoresins printer called Quantum X³, developed by Nanoscribe GmbH from Eggenstein-Leopoldshafen, Germany. This enables the synthetization of micro and nano structures made from acrylic resins, like IP-Dip and IP-S that have a known Young's modulus of 4,5–4,6 *GPa* [72].

After the acrylic designs were made, they go through a nanomagnetic particle coating process, resulting in a 1 *cm* × 1 *cm* disk covered with 100 cantilever-like structures with similar structure to the coated sperm cells as depicted in Figure 8.

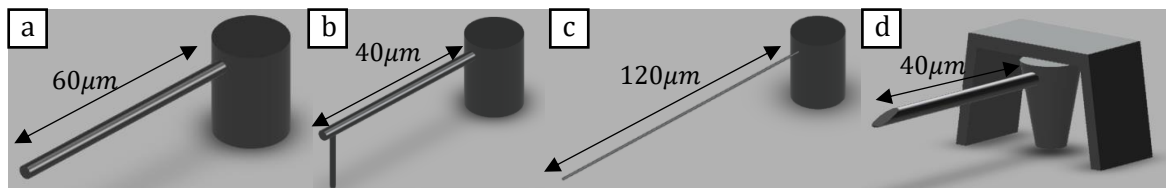


FIGURE 8 Four different cantilever structures that were printed using 2PL technology with posterior magnetic coating for external actuation. Of them all, the cantilever (a) showed more similarities to coated sperm cells. (a), (b), and (d) have 2 μm diameter radius, and (c) has 1 μm diameter radius.

During experimental realizations, all the different designs resulted in unreactive samples to external magnetic actuation, barely responding to the field exerted to their original form. It first was thought that the cantilevers were stuck to the ground of the lamina, but even after careful scraping of the bottom of the sample to try the release of the flagella, the cantilevers broke, and for a few seconds, they showed some reaction to the magnetic fields, but shortly after, the samples turned static.

Unfortunately, and after several trials, time was insufficient to come up with solutions and alternative designs to surpass this challenge. Despite this, and respecting all hydrodynamic properties, methods for creating this experiment in the millimetre scale are still being elaborated at the time of this work's completion.

³ <https://www.nanoscribe.com/en/products/quantum-x>

CHAPTER 3 – RESULTS

This chapter presents the results of the experimental work, along with various simulation approaches theorizing on the bending stiffness behaviour of all the configurations of SPINOSperm that helped taking conclusions on the experimental results that were posteriorly obtained.

3.1 SIMULATION RESULTS

To simulate the methods used for excitation of passive flagella described in the previous chapter, the following parameters were given to the MATLAB scripts: $\eta = 1 \text{ mPa}\cdot\text{s}$, $l = 60 \text{ }\mu\text{m}$, $d_f = 1 \text{ }\mu\text{m}$, $l_m = 13 \text{ }\mu\text{m}$, $l_p = 40 \text{ }\mu\text{m}$, and $l_d = 7 \text{ }\mu\text{m}$.

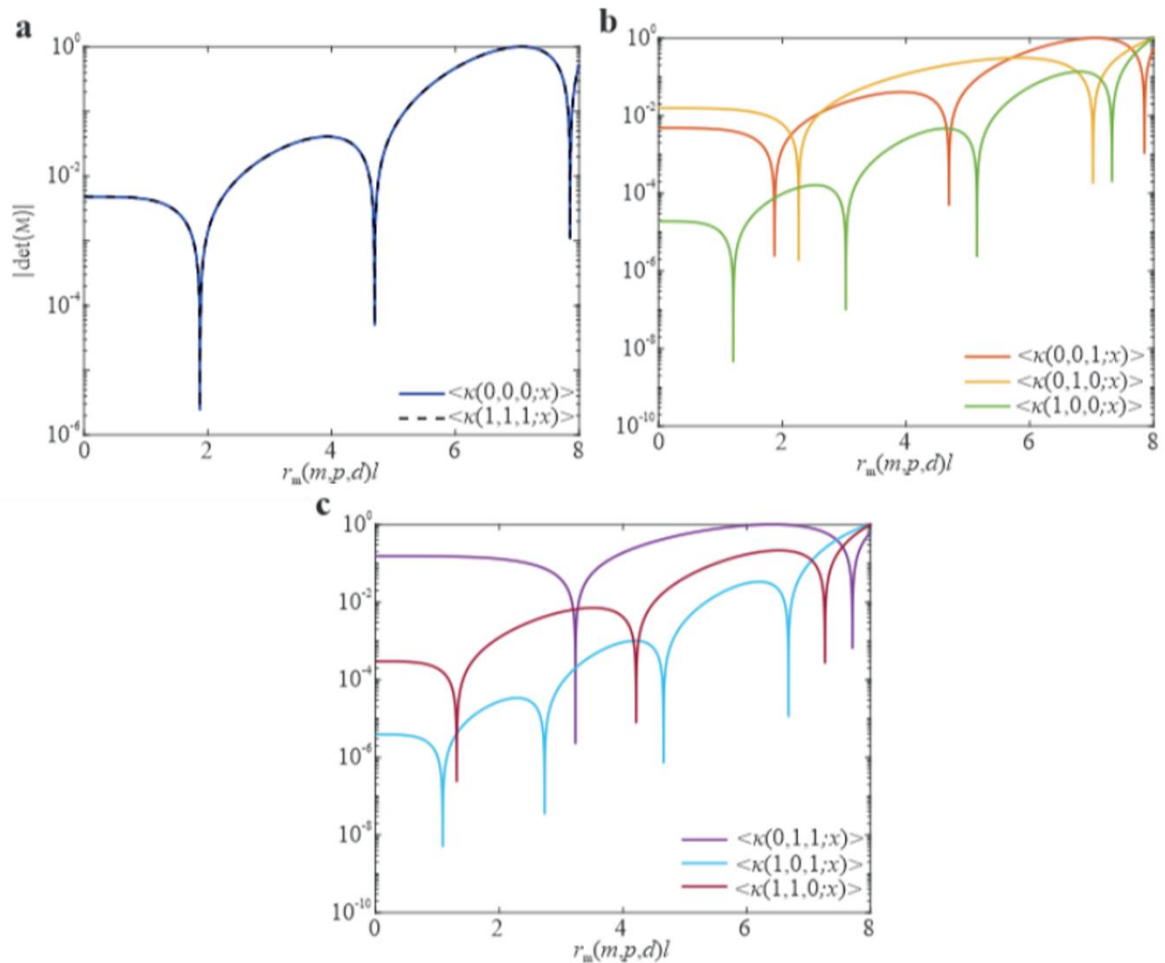


FIGURE 9 The absolute values of the determinant of \mathcal{M} are calculated versus $r_m(m,p,d)l$ for all groups. (a) For a fully uncoated and fully coated flagella. (b) For distal coated, principal piece coated, and midpiece coated flagella. (c) For flagella with two coated cellular segments. Adapted from Magdanz *et al.* (2021) [69].

For each type of magnetization, the local minima of $|\mathcal{M}|$ indicates non-trivial solutions of Equation (26). For each group, the first local minima at $r_m(m, p, d)l$ is then used with Equation (21) to get the relaxation constant τ .

From Figure 9(a), it is possible to note that the constant μ that minimizes $|\mathcal{M}|$ is approximately the same, but they differ in the decay time $\tau(m, p, d)$:

$$\langle \kappa(0,0,0) \rangle = 1.05 \times 10^{-18} \frac{\xi_{\perp}(x)}{\tau(0,0,0)};$$

$$\langle \kappa(1,1,1) \rangle = 1.05 \times 10^{-18} \frac{\xi_{\perp}(x)}{\tau(1,1,1)};$$

Then, from Figure 9(b)(c), it is possible to extract the values of $r_m(m, p, d)l$ for the other configurations:

$$r_m(0,0,1)l = 1.875; r_m(0,1,0)l = 2.266; r_m(1,0,0)l = 1.209;$$

$$r_m(0,1,1)l = 3.231; r_m(1,0,1)l = 1.086; r_m(1,1,0)l = 1.3127.$$

By using Equation (28):

$$\langle \kappa(0,0,1) \rangle = \kappa_m; \langle \kappa(0,1,0) \rangle = \left(\frac{2.266}{1.875} \right)^4 \kappa_m; \langle \kappa(1,0,0) \rangle = \left(\frac{1.209}{1.875} \right)^4 \kappa_m;$$

$$\langle \kappa(0,1,1) \rangle = \left(\frac{3.231}{1.875} \right)^4 \kappa_m; \langle \kappa(1,0,1) \rangle = \left(\frac{1.086}{1.875} \right)^4 \kappa_m; \langle \kappa(1,1,0) \rangle = \left(\frac{1.3127}{1.875} \right)^4 \kappa_m.$$

To simulate the decay time of the configuration $\tau(m, p, d)$, a magnetic torque is fed to the MATLAB program with a distribution of bending moment $\mathcal{B}(m, p, d; x)$. Additionally, the position of the simulating filament at $l, l/2$, and $l/4$ is determined in respect to time as the relaxation time is calculated from the slope of $\log(y)$. The results are described segment by segment as follows:

From Figure 10(c)(d)(g)(l), the decay times are extracted:

$$l/4 \rightarrow 1/\tau(0,0,0) = 0.64 \text{ s}^{-1}; l/2 \rightarrow 1/\tau(0,0,0) = 0.69 \text{ s}^{-1};$$

$$l \rightarrow 1/\tau(0,0,0) = 0.77 \text{ s}^{-1};$$

$$l/4 \rightarrow 1/\tau(1,1,1) = 7.17 \text{ s}^{-1}; l/2 \rightarrow 1/\tau(1,1,1) = 7.21 \text{ s}^{-1};$$

$$l \rightarrow 1/\tau(1,1,1) = 7.22 \text{ s}^{-1}.$$

The average decay times for these configurations are $1/\tau(0,0,0) = 0.7 \text{ s}^{-1}$ and $1/\tau(1,1,1) = 7.2 \text{ s}^{-1}$.

Feeding these results in Equations (27) and (28):

$$\langle \kappa(0,0,0) \rangle^{27} = 4.73 \times 10^{-21} \text{ N} \cdot \text{m}^2; \langle \kappa(0,0,0) \rangle^{28} = 4.73 \times 10^{-21} \text{ N} \cdot \text{m}^2;$$

$$\langle \kappa(1,1,1) \rangle^{27} = 16.38 \times 10^{-21} \text{ N} \cdot \text{m}^2; \langle \kappa(1,1,1) \rangle^{28} = 16.08 \times 10^{-21} \text{ N} \cdot \text{m}^2.$$

Then, the same process is repeated to all other configurations.

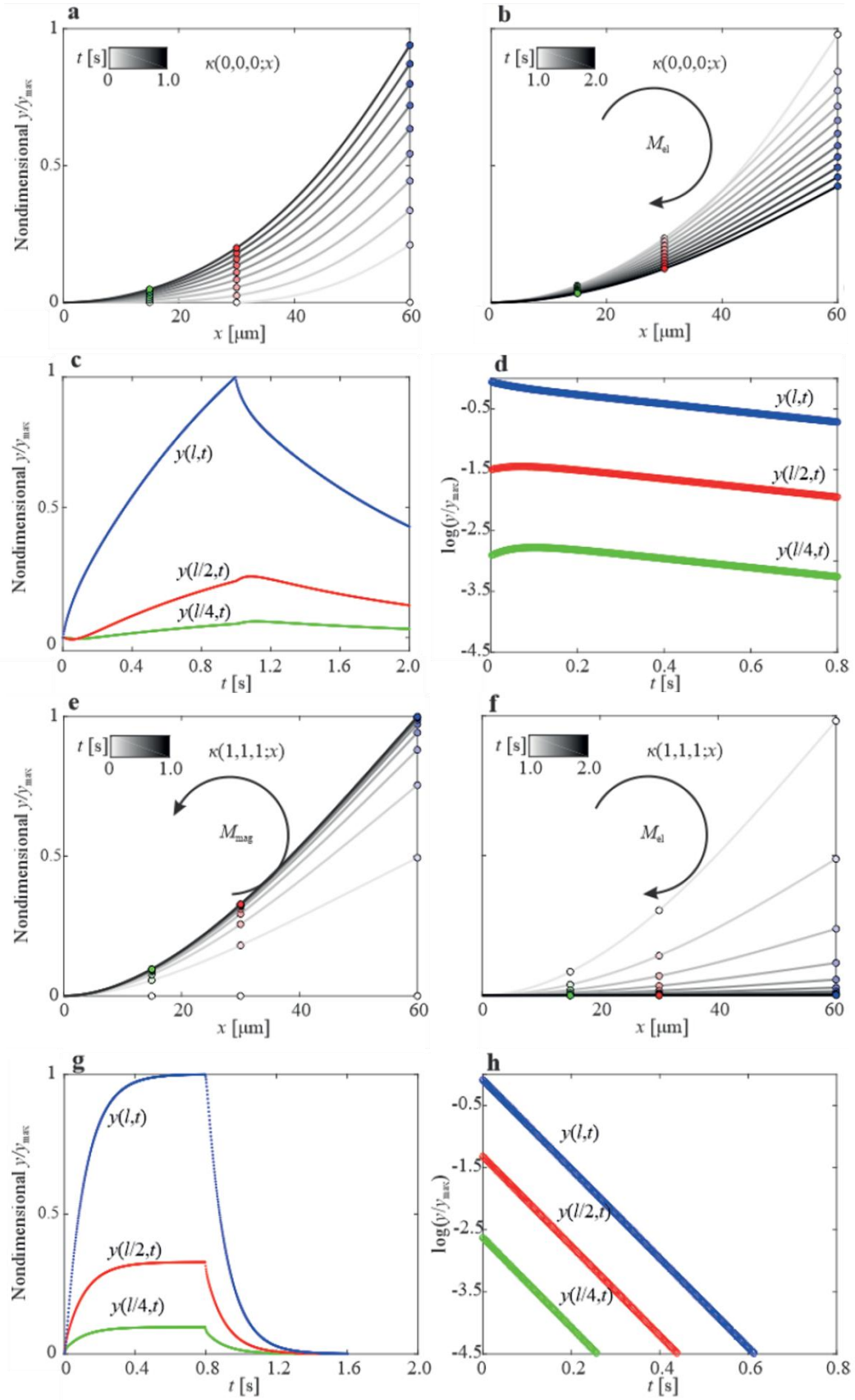
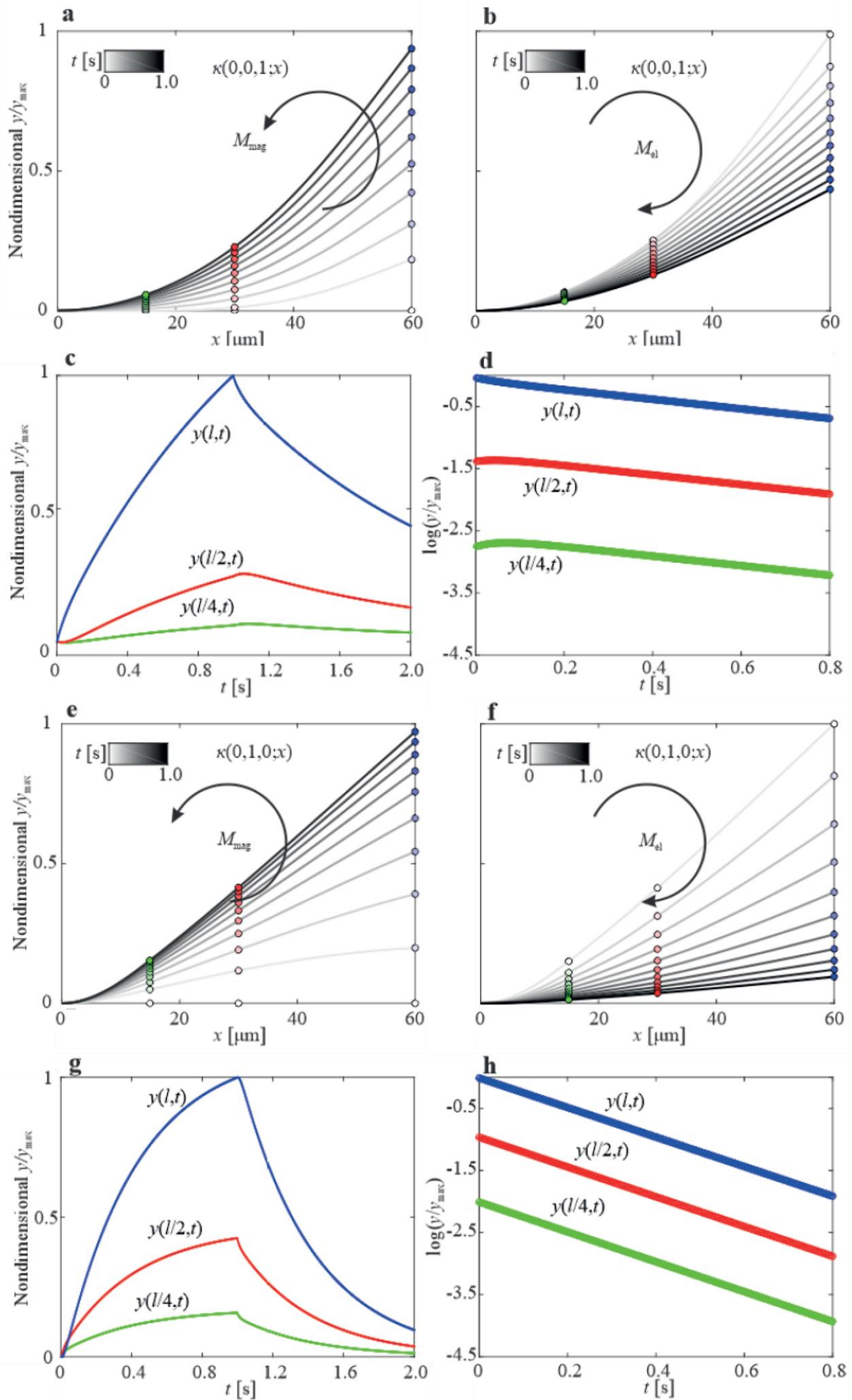


FIGURE 10 Simulation results for (0,0,0) (a–d) and (1,1,1) (e)–(h) configurations. Since there is no magnetic particles in the uncoated flagella, the distal end is considered dragged by a contact force and then removed so that the elastic moment restores it to the original position (a)–(b). Adapted from Magdanz *et al.* (2021) [69].

For 1 magnetized cellular segment:



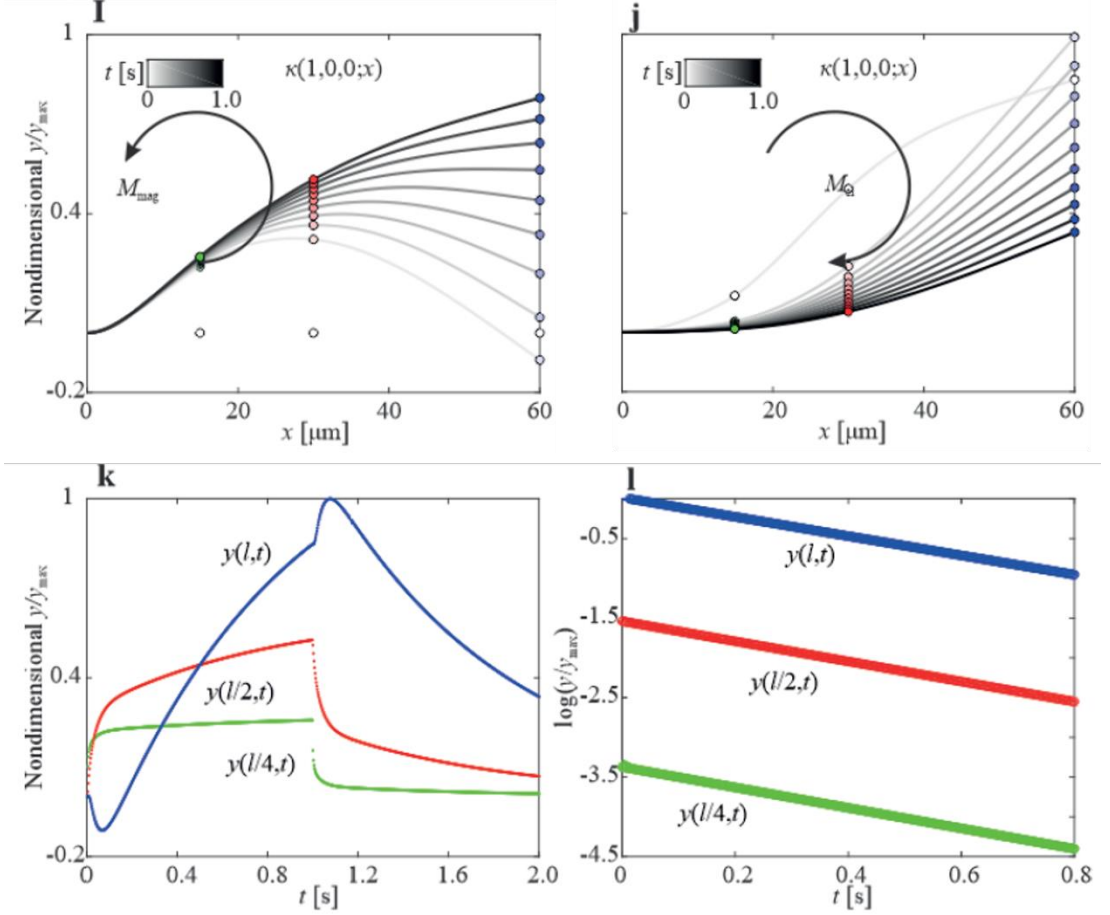


FIGURE 11 Simulation results for (0,0,1) (a)–(d), (0,1,0) (e)–(h) and (1,0,0) (i)–(l) configurations. Adapted from Magdanz *et al.* (2021) [69].

From Figure 11(c)(d)(g)(h)(k)(l), the decay times are extracted:

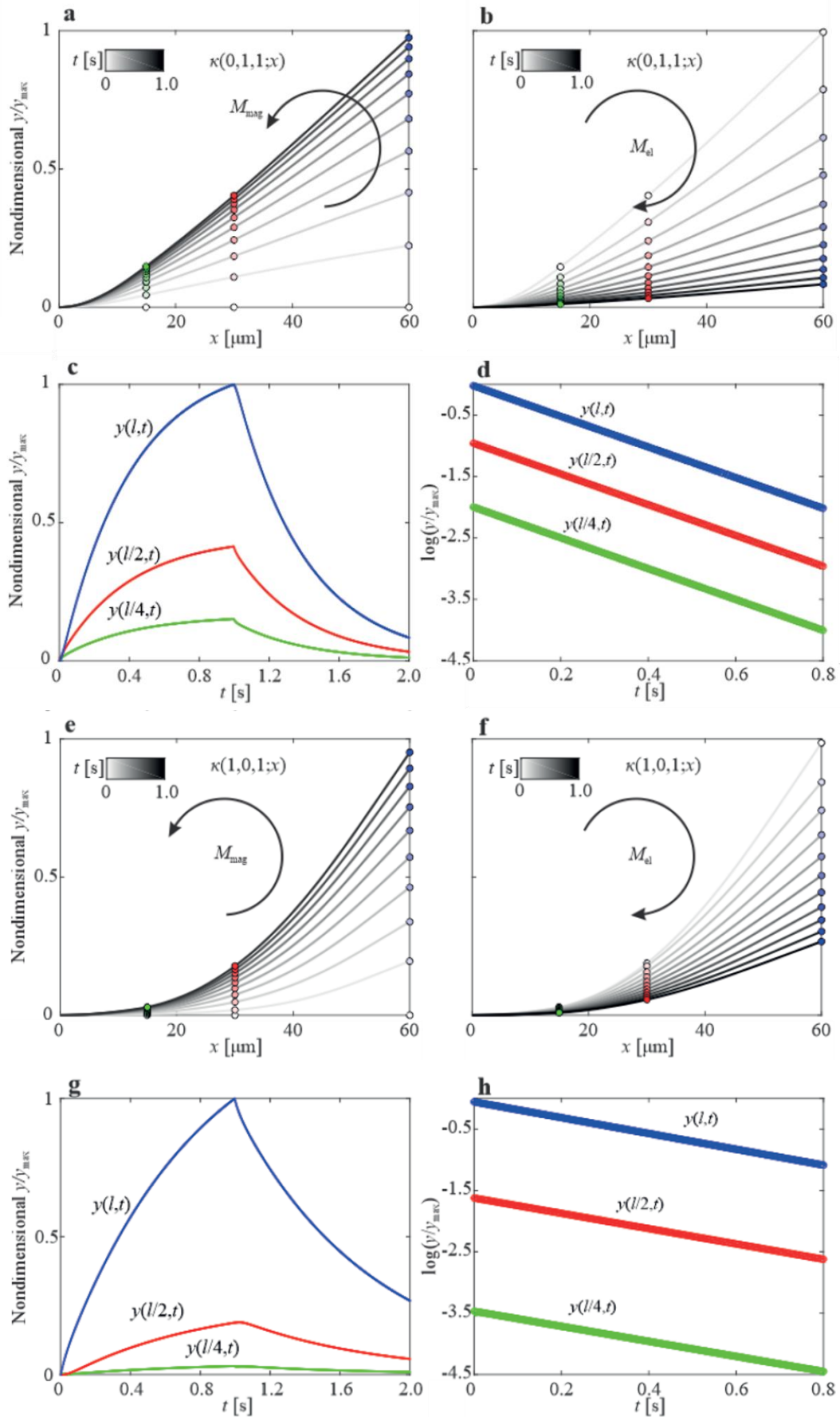
$$\begin{aligned}
 l/4 &\rightarrow 1/\tau(0,0,1) = 0.71 \text{ s}^{-1}; \quad l/2 \rightarrow 1/\tau(0,0,1) = 0.74 \text{ s}^{-1}; \\
 l &\rightarrow 1/\tau(0,0,1) = 0.78 \text{ s}^{-1}; \\
 l/4 &\rightarrow 1/\tau(0,1,0) = 2.40 \text{ s}^{-1}; \quad l/2 \rightarrow 1/\tau(0,1,0) = 2.39 \text{ s}^{-1}; \\
 l &\rightarrow 1/\tau(0,1,0) = 2.37 \text{ s}^{-1}; \\
 l/4 &\rightarrow 1/\tau(1,0,0) = 1.28 \text{ s}^{-1}; \quad l/2 \rightarrow 1/\tau(1,0,0) = 1.21 \text{ s}^{-1}; \\
 l &\rightarrow 1/\tau(1,0,0) = 1.21 \text{ s}^{-1}.
 \end{aligned}$$

The average decay times for these configurations are $1/\tau(0,0,1) = 0.74 \text{ s}^{-1}$, $1/\tau(0,1,0) = 2.38 \text{ s}^{-1}$, and $1/\tau(1,0,0) = 1.25 \text{ s}^{-1}$.

Feeding these results in Equations (27) and (28):

$$\begin{aligned}
 \langle \kappa(0,0,1) \rangle^{27} &= 6.24 \times 10^{-21} \text{ N} \cdot \text{m}^2; \quad \langle \kappa(0,0,1) \rangle^{28} = 4.61 \times 10^{-21} \text{ N} \cdot \text{m}^2; \\
 \langle \kappa(0,1,0) \rangle^{27} &= 8.28 \times 10^{-21} \text{ N} \cdot \text{m}^2; \quad \langle \kappa(0,1,0) \rangle^{28} = 8.06 \times 10^{-21} \text{ N} \cdot \text{m}^2; \\
 \langle \kappa(1,0,0) \rangle^{27} &= 4.72 \times 10^{-21} \text{ N} \cdot \text{m}^2; \quad \langle \kappa(1,0,0) \rangle^{28} = 6.42 \times 10^{-21} \text{ N} \cdot \text{m}^2.
 \end{aligned}$$

Finally, for two magnetized cellular segments:



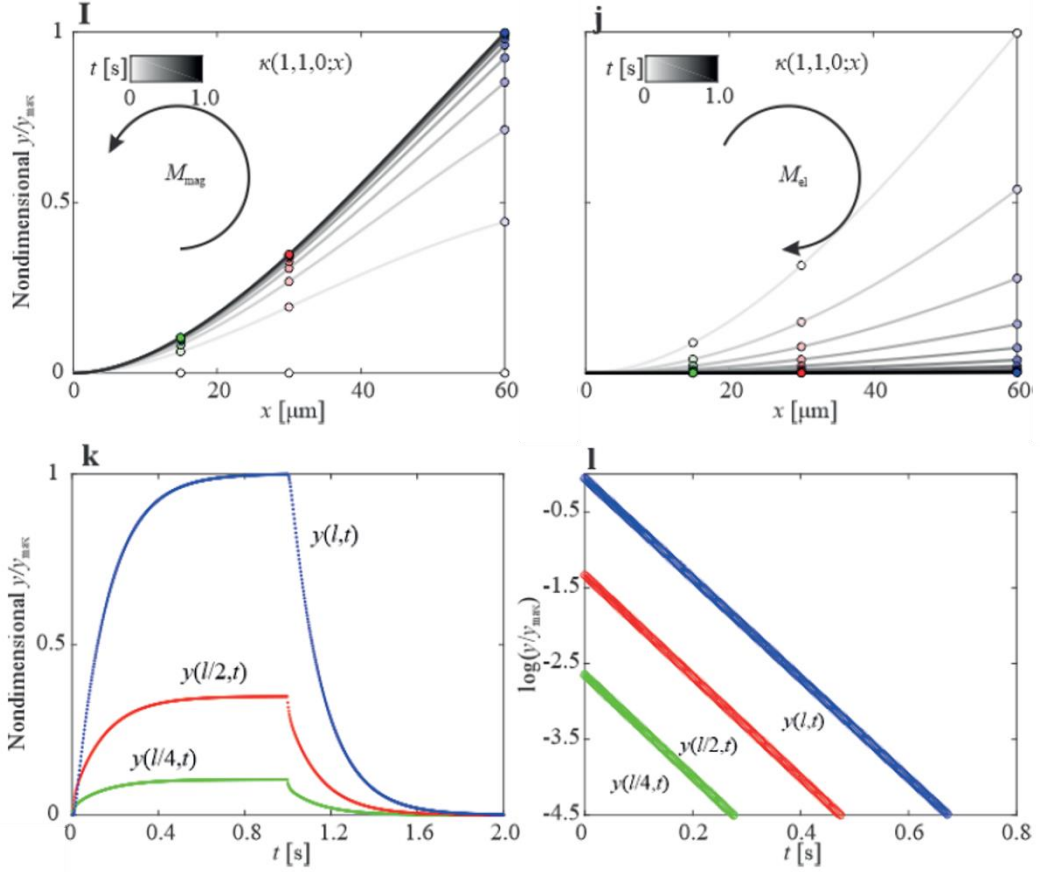


FIGURE 12 Simulation results for (0,1,1) (a)–(d), (1,0,1) (e)–(h), and (1,1,0) (i)–(l) configurations. Adapted from Magdanz *et al.* (2021) [69].

From Figure 12(c)(d)(g)(h)(k)(l), the decay times are extracted:

$$l/4 \rightarrow 1/\tau(0,1,1) = 2.51 \text{ s}^{-1}; \quad l/2 \rightarrow 1/\tau(0, q, 1) = 2.50 \text{ s}^{-1};$$

$$l \rightarrow 1/\tau(0, q, 1) = 2.48 \text{ s}^{-1};$$

$$l/4 \rightarrow 1/\tau(1,0,1) = 1.22 \text{ s}^{-1}; \quad l/2 \rightarrow 1/\tau(1,0,1) = 1.24 \text{ s}^{-1};$$

$$l \rightarrow 1/\tau(1,0,1) = 1.28 \text{ s}^{-1};$$

$$l/4 \rightarrow 1/\tau(1,1,0) = 6.71 \text{ s}^{-1}; \quad l/2 \rightarrow 1/\tau(1,1,0) = 6.68 \text{ s}^{-1};$$

$$l \rightarrow 1/\tau(1,1,0) = 6.59 \text{ s}^{-1}.$$

The average decay times for these configurations are $1/\tau(0,1,1) = 2.5 \text{ s}^{-1}$, $1/\tau(1,0,1) = 1.25 \text{ s}^{-1}$, and $1/\tau(1,1,0) = 6.6 \text{ s}^{-1}$.

Feeding these results in Equations (27) and (28):

$$\langle \kappa(0,1,1) \rangle^{27} = 16.34 \times 10^{-21} \text{ N} \cdot \text{m}^2; \quad \langle \kappa(0,1,1) \rangle^{28} = 16.03 \times 10^{-21} \text{ N} \cdot \text{m}^2;$$

$$\langle \kappa(1,0,1) \rangle^{27} = 6.54 \times 10^{-21} \text{ N} \cdot \text{m}^2; \quad \langle \kappa(1,0,1) \rangle^{28} = 4.64 \times 10^{-21} \text{ N} \cdot \text{m}^2;$$

$$\langle \kappa(1,1,0) \rangle^{27} = 8.29 \times 10^{-21} \text{ N} \cdot \text{m}^2; \quad \langle \kappa(1,1,0) \rangle^{28} = 8.08 \times 10^{-21} \text{ N} \cdot \text{m}^2.$$

ACTUATION FREQUENCY

It is well known that a sperm number of 2.1 gives the optimal swimming parameters for transverse-wave propulsion in low- Re . This sperm number is highly influenced by the swimmer's properties namely length, bending stiffness and actuation frequency, as seen in Equation (4). The length of this soft microrobot is fixed since it depends on the length of the sperm cell's flagellum, so the only manipulable variables remaining are the bending stiffness and actuation frequency.

As shown below in Figure 13, these two properties are directly proportional to each other suggesting that a filament can be made very flexible and actuated at low frequencies or relatively stiff and actuated at high frequencies to produce the same maximum propulsive thrust $\langle f \rangle$. Thus, further research is necessary to investigate the influence of the nanoparticle coating in the optimal actuation frequency, ω , for $Sp = 2.1$, which consequently influences the propulsive thrust of the microrobots.

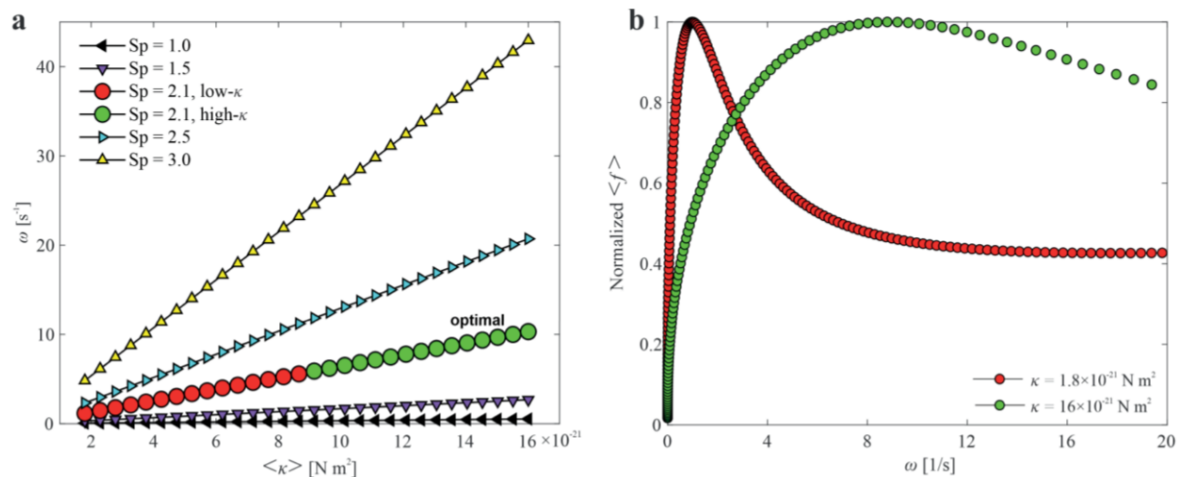


FIGURE 13 Actuation frequency, ω , of a magnetizable segment is calculated for different bending stiffness, κ , and sperm number, Sp , using Equation (4). (a) For optimal flagellar propulsion ($Sp = 2.1$), the optimal actuation frequency is directly proportional to the averaged bending stiffness over the length. (b) Optimal propulsive time-averaged thrust force, $\langle f \rangle$, of a flagellum with greater bending stiffness is achieved at higher actuation frequency [68]. Improvement of the frequency response is achieved for flagellum with greater bending stiffness. Adapted from Magdanz *et al.* (2021) [69].

3.2 EXPERIMENTAL RESULTS

After the precipitation of the cells in the lamina, a suitable configuration is found and excited with a magnetic field of 5 mT with 3 different small angles: $\theta = 0^\circ$, 5° , and 15° , between the long axis of the cell e_1 and the direction of applied magnetic field. Since the nanoparticle coating process is very random, the search for these targeted configurations is sometimes difficult and time consuming.

Nevertheless, once a configuration is found and actuated, at $t = 0$ s, the magnetic field is turned off and the flagellum returns to its original position. Then the magnetic field is turned on again, the flagellum goes to its excited position, and then the magnetic field is turned off again, repeating this process 10 times for each one of the 3 angles, sometimes even more angles were done. Figure 14 shows an example of this excitation method being applied.

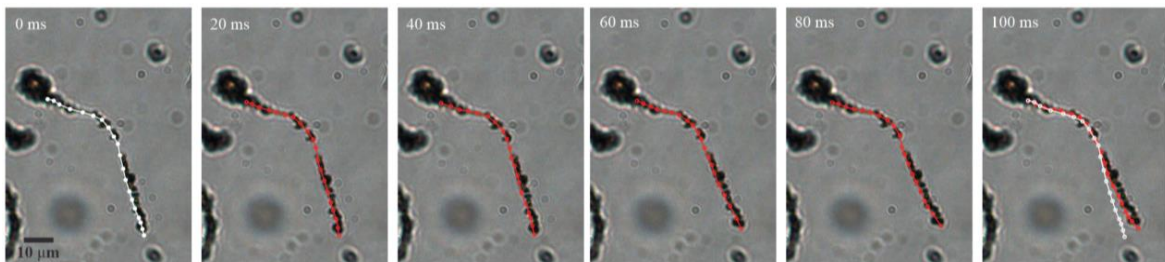


FIGURE 14 Nanoparticle coated sperm cell with its head fixed to a solid boundary is actuated. At $t = 0$ s, the applied magnetic field is removed, and the flagellum restores to its original position. Adapted from Magdanz *et al.* (2021) [69].

Once all the videos for all configurations of SPINOSperm were done, the videos are fed to the MATLAB scripts, cropped and separated into frames so that the time of the relaxation of the tail can be accurately determined. After that, points are manually marked in the tail for each frame to measure the displacement of the flagellum relative to the previous frame. A representation of this marking system can also be seen in Figure 14. After running all the marked frames, the script shows the value of the decay time, τ , and the bending stiffness, κ , for the flagellum of the configuration analysed, using Equation (27). Additionally, to ensure minimal error, the maximum possible experiments were conducted for the configurations found, as the number of experiments conducted varies from configuration to configuration due unknown gradually unreactive or unviable excitations.

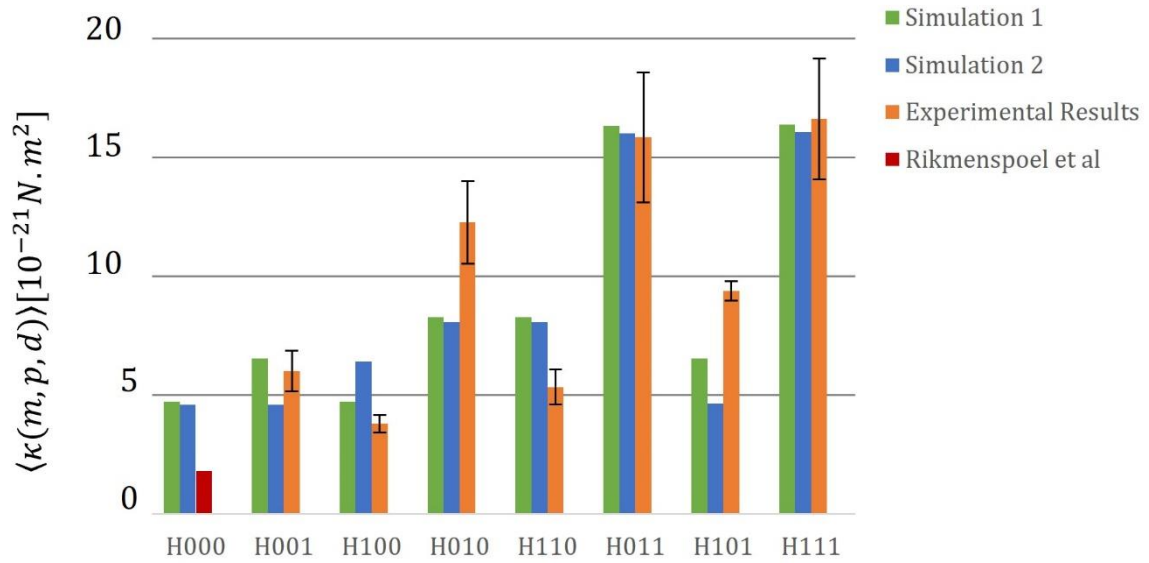


FIGURE 15 Bar plot with summarized results for Simulation 1 using Equations (11) and (27), Simulation 2 with Equation (28), measured bending stiffness using Equation (27), and reference value from [70].

A graphic with the summarized results can be found below in Figure 15, and for a better comprehension of the results, Table 1 provides the numerical values of the experimental results.

TABLE 1 Summarized table of the results with relaxation time, τ [s], and average bending stiffness, $\langle \kappa \rangle [N \cdot m^2]$, of the various possible configurations of nanoparticle coated sperm cells with their correspondents standard deviations.

Configuration	H000	H001	H100	H010	H110	H011	H101	H111
τ [s]	2,0	0,25 ± 0,04	0,97 ± 0,10	0,23 ± 0,01	0,78 ± 0,13	0,15 ± 0,10	0,28 ± 0,01	0,25 ± 0,04
$\langle \kappa \rangle [N \cdot m^2] \times 10^{-21}$	1,8	6,01 ± 0,85	3,79 ± 0,38	12,27 ± 1,73	5,34 ± 0,74	15,86 ± 2,74	9,39 ± 0,42	16,61 ± 2,54

As it is observed in both graphic and table, the average bending stiffness for one magnetized cellular segment varies significantly from cellular segment to cellular segment, and it is to some extent different from the results obtained in the simulation. In other words, although the experimental results of other configurations for one magnetized cellular segment are more in sync with the simulations, the experimental results obtained for the bending stiffness of (0,1,0) configuration differs quite a lot from the simulation result for the same configuration.

By the same unknown reason, this result can also be observed in the two magnetized cellular segment group, as the bending stiffness value for the (1,0,1) configuration is quite higher the values obtained through the simulations, and oppositely, the average bending stiffness for (1,1,0) configuration is lower than the simulations results.

In the other hand, the experimental values of the average bending stiffness for (0,0,1), (0,1,1), and (1,1,1) configurations reasonably approach the values that were given by the simulations results for the same magnetized cellular segments.

In the case of the non-magnetized cellular segment, the simulation values were compared with the results obtained by Rikmenspoel et al. (1966) in his determination of the bending stiffness using micro tweezers. The discrepancy in the values observed in the graphic may exist because of the excitation of the flagella of sea urchin spermatozoa was done with direct contact with the micro tweezers.

Although the reasons for the observed differences between experimental results and the simulations obtained values are a bit unknown, one possible reason for this may be because the lack of significantly number of experimental trials for the different possible configurations. For instance, the number of samples experimented for the (1,1,1) configuration, which has a very fine agreement with the simulation results, is 3 times higher than the number of experiments for the (0,1,1) configuration, which has low agreement between experimental and simulation results.

Nevertheless, from these simulation and experimental results, it is possible to conclude that the magnetization of the flagellum affects its intrinsic bending stiffness. Moreover, the location of the magnetic coating also displays serious effect as the variation of bending stiffness between samples with the same number of coated segments. Furthermore, among the 3 cellular segments of the flagella, the one that most contributes to an increase in bending stiffness, when coated, is the principal piece.

CHAPTER 4 – CONCLUSION

This work found that it is possible to determine the apparent bending stiffness of nanoparticle coated bull sperm cells using a magnetic excitation method with minimal risk of damage during the characterization. These soft biohybrid microrobots were made by electrostatic self-assembly of magnetic nanoparticles and bull sperm cells, which due to the magnetic coating have their intrinsic bending stiffness of the flagellum increased.

The overall results backed up with theoretical predictions and simulations show that the bending stiffness for every possible configuration of these magnetic soft microrobots are well defined and differ from group to group according to the location of the magnetic coating along the flagellum. Additionally, the two electromagnetic coils enabled a contactless magnetic actuation method for the excitation of the microswimmers' flagella without causing additional influence, hence highly limiting the damage made to the tail that would otherwise happen if the excitation method used direct contact to the flagella, which is the case of previous similar studies.

In summary, it is proved by both theoretical and experimental results that the average bending stiffness of passive flagella varies proportionally to the location of magnetized cellular segments for all seven considered groups, and it has a minimum value of $\langle \kappa \rangle = (3.79 \pm 0.37) \times 10^{-21} \text{ N.m}^2$ for (1,0,0) configuration, and a maximum value of $\langle \kappa \rangle = (16.61 \pm 2.54) \times 10^{-21} \text{ N.m}^2$ for the fully coated flagellum, which is more than four times higher.

Despite the fact that some expectations for this study were not achieved, such as the general high agreement between all simulations results and experimental values for the average bending stiffness of all the groups, as well as the lack for a functional control group for the excitation method used, the discoveries made from this experiments are a major contribution to the microrobotics field regarding the locomotion in low- Re fluidic environments, and set clearly what the next steps should be in the pursuit for the perfect microswimmer that will revolutionize Minimal Invasive Medical Applications.

REFERENCES

- [1] Tendick, F. Sastry, S. S., Fearing, R. S. and Cohn, M. (1998). Applications of micromechanics in minimally invasive surgery. *IEEE/ASME Transactions Mechatronics*.
- [2] Palagi, S. and Fischer, P. (2018). Bioinspired microrobots. *Nature Reviews Materials*.
- [3] Nelson, B.J., Kaliakatsos, I.K. and Abbott, J.J. (2010). Microrobots for Minimally Invasive Medicine. *Annual Review of Biomedical Engineering*.
- [4] Alapan, Y., Yasa, O., Ygit, B., Yasa, I. C., Erkoc, P. and Sitti, M. (2019). Microrobotics and Microorganisms: Biohybrid Autonomous Cellular Robots. *Annual Review of Control, Robotics, and Autonomous Systems*.
- [5] Kassim, I., Phee, L., Ng, W. S., Gong, F., Dario, P. and Mosse, C. A. (2006). Locomotion techniques for robotic colonoscopy. *IEEE Engineering in Medicine and Biology Magazine*.
- [6] Sonntag, L., Simmchen, J. and Magdanz V. (2019). Nano-and Micromotors Designed for Cancer Therapy. *Molecules*.
- [7] Wautelet, M. (2001). Scaling laws in the macro-, micro- and nanoworlds. *European Journal of Physics*.
- [8] Purcell, E. M. (1977). Life at low Reynolds-number. *American Journal of Physics*.
- [9] Sznitman, J., Shen, X., Sznitman, R. and Arratia, P. E. (2010). Propulsive force measurements and flow behavior of undulatory swimmers at low Reynolds number. *Physics of Fluids*.
- [10] Machin, K. E. (1958). Wave propagation along flagella. *Journal of Experimental Biology*.
- [11] Coq, N., du Roure, O., Fermigier, M. and Bartolo, D. (2009). Helical beating of an actuated elastic filament. *Journal of Physics: Condensed Matter*.
- [12] Behkam, B. and Sitti, M. (2006). Design methodology for biomimetic propulsion of miniature swimming robots. *Journal of Dynamic Systems, Measurement, and Control*.
- [13] Kósa, G., Shoham, M. and Zaaroor, M. (2007). Propulsion method for swimming microrobots. *IEEE Transactions on Robotics*.
- [14] Kósa, G., Jakab, P., Jólesz, F. and Hata, N. (2008). Swimming capsule endoscope using static and RF magnetic field of MRI for propulsion. *Proceedings - International*

IEEE Conference on Robotics and Automation.

[15] Yu, T. S., Lauga, E. and Hosoi, A. E. (2006). Experimental investigations of elastic tail propulsion at low Reynolds number. *Physics of Fluids*.

[16] Gray, J. and Hancock, G. J. (1955). The propulsion of sea-urchin spermatozoa. *Journal of Experimental Biology*.

[17] Friedrich, B. M., Riedel-Kruse, I. H., Howard, J. and Julicher, F. (2010). High-precision tracking of sperm swimming fine structure provides strong test of resistive force theory. *Journal of Experimental Biology*.

[18] Khalil, I. S. M., Klingner, A. and Misra, S. (2020). Mathematical Modeling of Soft Microswimmers.

[19] Gillies, G. T., Ritter, R. C., Broaddus, W. C., Grady, M. S., Howard, M. A. III and McNeil, R. G. (1994). Magnetic manipulation instrumentation for medical physics research. *Review of Scientific Instruments*.

[20] Mathieu, J-B., Beaudoin, G. and Martel, S. (2006). Method of propulsion of a ferromagnetic core in the cardiovascular system through magnetic gradients generated by an MRI system. *IEEE Transactions on Biomedical Engineering*.

[21] Martel, S., Mathieu, J-B., Felfoul, O., Chanu, A., Aboussouan, E., et al. (2007). Automatic navigation of an untethered device in the artery of a living animal using a conventional clinical magnetic resonance imaging system. *Applied Physics Letter*.

[22] Grady, M. S., Howard, M. A. III, Molloy, J. A., Ritter, R. C., Quate, E. G. and Gillies, G. T. (1990). Nonlinear magnetic stereotaxis: three-dimensional, in vivo remote magnetic manipulation of a small object in canine brain. *Medical Physics*.

[23] Meeker, D. C., Maslen, E. H., Ritter, R. C. and Creighton, F. M. (1996). Optimal realization of arbitrary forces in a magnetic stereotaxis system. *IEEE Transactions on Magnetics*.

[24] Yesin, K. B., Vollmers, K. and Nelson, B. J. (2006). Modeling and control of untethered biomicrorobots in a fluidic environment using electromagnetic fields. *International Journal of Robotics Research*.

[25] Magdanz, V., Khalil, I. S., Simmchen, J., Furtado, G. P., Mohanty, S., Gebauer, J., Xu, H., Klingner, A., Aziz, A., Medina-Sánchez M., et al. (2020). IRONSperm: Sperm-templated soft magnetic microrobots. *Science Advances*.

[26] Kalambur, V. S., Han, B., Hammer, B.E., Shield, T. W. and Bischof, J. C. (2005). In vitro characterization of movement, heating and visualization of magnetic nanoparti-

cles for biomedical applications. *Nanotechnology*.

[27] Martel, S., Mohammadi, M., Felfoul, O., Zhao, L. and Pouponneau, P. (2009). Flagellated magnetotactic bacteria as controlled MRI-trackable propulsion and steering systems for medical nanorobots operating in the human microvasculature.

International Journal of Robotics.

[28] Northern Digital Inc. (2020). The Aurora Electromagnetic Measurement System. Available at: <https://www.ndigital.com/products/aurora/> [Accessed 13 Sep. 2021].

[29] Hu, C., Meng, M. Q.-H. and Mandal, M. (2005). Efficient magnetic localization and orientation technique for capsule endoscopy. *International Journal of Information Acquisition*.

[30] Antonuk, L. E., Jee, K.-W., El-Mohri, Y., Maolinbay, M, and Nassif, S., et al. (2000). Strategies to improve the signal and noise performance of active matrix, flat-panel imagers for diagnostic X-ray applications. *Medical Physics*.

[31] Duryea, J., Magalnick, M., Alli, S., Yao, L., Wilson, M. and Goldbach-Mansky, R. (2008). Semiautomated three dimensional segmentation software to quantify carpal bone volume changes on wrist CT scans for arthritis assessment. *Medical Physics*.

[32] Felfoul, O., Martel, S., Beaudoin, G. and Mathieu, J.-B. (2004). Microdevice's susceptibility difference-based MRI positioning system, a preliminary investigation. *Proceedings of the Annual International Conference of the IEEE Engineering in Medicine and Biology Society, San Francisco, California, USA, September*.

[33] Flückiger, M. and Nelson, B. J. (2007). Ultrasound emitter localization in heterogeneous media. *Proceedings of the Annual IEEE International Conference Engineering in Medicine and Biology Society, Lyon, France, August*.

[34] Rubinstein, L. (2000). A practical nanorobot for treatment of various medical problems. *Presented at Eighth Foresight Conference on Molecular Nanotechnologies*.

[35] Devlin, P. M. (2007). Brachytherapy: Applications and Techniques. *Philadelphia: Lippincott Williams & Wilkins*.

[36] Andrä, W., Nowak, H. (2007). Magnetism in Medicine: A Handbook. *Weinheim, Germany: Wiley-VCH*.

[37] Zhang, H., Hutmacher, D. W., Chollet, F., Poo, A.-N. and Burdet, E. (2005). Microrobotics and MEMS-based fabrication techniques for scaffold-based tissue engineering. *Macromolecular Biosciences*.

- [38] Berger, S. A., Goldsmith, W. and Lewis, E. R. (1996). Introduction to Bioengineering. *Oxford, UK: Oxford University Press.*
- [39] Zaaroor, M., Kósa, G., Peri-Eran, A., Maharil, I., Shoham, M. and Goldsher, D. (2006). Morphological study of the spinal canal content for subarachnoid endoscopy. *Minimal Invasive Neurosurgery.*
- [40] Duffner, F., Schiffbauer, H., Glemser, D., Skalej, M. and Freudenstein, D. (2003). Anatomy of the cerebral ventricular system for endoscopic neurosurgery: a magnetic resonance study. *Acta Neurochirurgica.*
- [41] Renner, C. and Rassweiler J. (1999). Treatment of renal stones by extracorporeal shock wave lithotripsy. *Nephron.*
- [42] Edd, J., Payen, S., Rubinsky, B., Stoller, M. L. and Sitti, M. (2003). Biomimetic propulsion for a swimming surgical micro-robot. *Proceedings of the IEEE/RSJ International Conference on Intelligent Robots and Systems, Las Vegas, November.*
- [43] Kristo, B., Liao, J. C., Neves, H. P., Churchill, B. M., Montemagno, C. D. and Schulam, P. G. (2003). Microelectromechanical systems in urology. *Urology.*
- [44] Flake, A. W. (2003). Surgery in the human fetus: the future. *Journal of Physiology.*
- [45] Berris, M. and Shoham, M. (2006). Febotics—a marriage of fetal surgery and robotics. *Computer Aided Surgery.*
- [46] Jagtap, A. D. and Riviere, C. N. (2004). Applied force during vitreoretinal microsurgery with handheld instruments. *Proceedings of the Annual International Conference of the IEEE Engineering in Medicine and Biology Society, San Francisco, California, USA, September.*
- [47] Gupta, P. K., Jensen, P. S. and de Juan, E. Jr. (1999). Surgical forces and tactile perception during retinal microsurgery. *Lecture Notes in Computer Science.*
- [48] Stratigouleas, E. D., Perry, B. P., King, S. M. and Syms, C. A. III. (2006). Complication rate of minimally invasive cochlear implantation. *Otolaryngology Head Neck Surgery.*
- [49] Parker, M. A. and Cotanche, D. A. (2004). The potential use of stem cells for cochlear repair. *Audiology and Neurotology.*
- [50] Gao, W., Feng, X., Pei, A., Kane, C.R., Tam, R., Hennessy, C. and Wang, J. (2013). Bioinspired Helical Microswimmers Based on Vascular Plants. *Nano Letters.*
- [51] Williams, B.J., Anand, S.V., Rajagopalan, J. and Saif, M.T.A. (2014). A self-propelled biohybrid swimmer at low Reynolds number. *Nature Communications.*

- [52] Sahari, A., Traore, M.A., Scharf, B.E. and Behkam, B. (2014). Directed transport of bacteria-based drug delivery vehicles: bacterial chemotaxis dominates particle shape. *Biomedical Microdevices*.
- [53] Zhuang, J., Wright Carlsen, R. and Sitti, M. (2015). pH-Taxis of Biohybrid Microsystems. *Scientific Reports*.
- [54] Srivastava, S.K., Medina-Sánchez, M., Koch, B. and Schmidt, O.G. (2015). Medibots: Dual-Action Biogenic Microdaggers for Single-Cell Surgery and Drug Release. *Advanced Materials*.
- [55] Felfoul, O., Mohammadi, M., Taherkhani, S., de Lanauze, D., Zhong Xu, Y., Loghin, D., Essa, S., Jancik, S., Houle, D., Lafleur, M., Gaboury, L., Tabrizian, M., Kaou, N., Atkin, M., Vuong, T., Batist, G., Beauchemin, N., Radzioch, D. and Martel, S. (2016). Magneto-aerotactic bacteria deliver drug-containing nanoliposomes to tumour hypoxic regions. *Nature Nanotechnology*.
- [56] Khalil, I. S. M., Fatih Tabak, A., Klingner, A. and Sitti, M. (2016). Magnetic propulsion of robotic sperms at low-Reynolds number. *Applied Physics Letters*.
- [57] Xu, H., Medina-Sánchez, M., Magdanz, V., Schwarz, L., Hebenstreit, F. and Schmidt, O.G. (2017). Sperm-Hybrid Micromotor for Targeted Drug Delivery. *ACS Nano*.
- [58] Yasa, O., Erkoc, P., Alapan, Y. and Sitti, M. (2018). Microalga-Powered Microswimmers toward Active Cargo Delivery. *Advanced Materials*.
- [59] Sun, M., Fan, X., Meng, X., Song, J., Chen, W., Sun, L. and Xie, H. (2019). Magnetic biohybrid micromotors with high manoeuvrability for efficient drug loading and targeted drug delivery. *Nanoscale*.
- [60] Lindemann, C.B., Rudd, W.G. and Rikmenspoel, R. (1973). The Stiffness of the Flagella of Impaled Bull Sperm. *Biophysical Journal*.
- [61] Harada, Y., Ota, T. and Takamatsu, T. (2007). Measurement of Young's modulus of primary cilia by using optical tweezers. 2007 International Symposium on Micro-NanoMechatronics and Human Science.
- [62] Hill, D. B., Swaminathan, V., Estes, A., Cribb, J., O'Brien, E. T., Davis, C. W. and Superfine, R. (2010). Force Generation and Dynamics of Individual Cilia under External Loading. *Biophysical Journal*.
- [63] Xu, G., Wilson, Kate S., Okamoto, Ruth J., Shao, J.-Y., Dutcher, Susan K. and Bayly, Philip V. (2016). Flexural Rigidity and Shear Stiffness of Flagella Estimated from Induced Bends and Counterbends. *Biophysical Journal*.

- [64] Xu, T., Zhang, J., Salehizadeh, M., Onaizah, O. and Diller, E. (2019). Millimetre-scale flexible robots with programmable three-dimensional magnetization and motions. *Science Robotics*.
- [65] Khalil, I. S. M., Magdanz, V., Simmchen, J., Klingner, A. and Misra, S. (2020). Resemblance between motile and magnetically actuated sperm cells. *Applied Physics Letters*.
- [66] Magdanz, V., Vivaldi, J., Mohanty, S., Klingner, A., Vendittelli, M., Simmchen, J., Misra, S. and Khalil, I. S. M. (2021). Impact of Segmented Magnetization on the Flagellar Propulsion of Sperm-Templated Microrobots. *Advanced Science*.
- [67] Magdanz, V., Gebauer, J., Sharan, P., Eltoukhy, S., Voigt, D. and Simmchen, J. (2019). Sperm-particle interactions and their prospects for charge mapping. *Advance Biosystems*.
- [68] Baqiya, M. A., Taufiq, A., Sunaryono, Ayun, K., Zainuri, M., Pratapa, S., Triwikantoro and Darminto. (2017). Spinel-Structured Nanoparticles for Magnetic and Mechanical Applications. *Magnetic Spinel - Synthesis, Properties and Applications*.
- [69] Magdanz, V., Estima, D., Dias, J. M. S., Punte, H., Klingner, A., Marques, L., Smith, D. and Khalil, I. S. M. (2021). Characterization of the Passive Bending Stiffness of Nanoparticle-Coated Sperm Cells using Magnetic Excitation. *(Under Review)*.
- [70] Rikmenspoel, R. (1966). Elastic Properties of the Sea Urchin Sperm Flagellum. *Biophysical Journal*.
- [71] Lemma, E., Rizzi, F., Sileo, L., Spagnolo, B., Dattoma, T., Qualtieri, A., De Vittorio, M. and Pisanello, F. (2015). Static and Dynamic Mechanical Characterization of Two-photon Lithography Photoresists. *Conference: Micro and Nanoengineering MNE 2015, Den Haag, Netherlands*.
- [72] Liu, Y., Campbell, J., Stein, O., Jiang, L., Hund, J. and Lu, Y. (2018). Deformation Behavior of Foam Laser Targets Fabricated by Two-Photon Polymerization. *Nanomaterials*.

APPENDICES

APPENDIX A – TABLES

TABLE(A) 1 Summarized data extracted from experiment 16 with H001 configuration. With length, $L[\mu m]$, relaxation time, $\tau[s]$, and average bending stiffness, $\langle\kappa\rangle[N.m^2]$, and their respective standard deviations.

H001	$L[\mu m]$	$\langle L \rangle[\mu m]$	$\tau[s]$	$\delta\tau[s]$	$\langle\tau\rangle[s]$	$\langle\delta\tau\rangle[s]$	$\kappa[N.\mu m^2]$	$\delta\kappa[N.\mu m^2]$	$\langle\kappa\rangle[N.\mu m^2]$	$\delta\langle\kappa\rangle[N.\mu m^2]$
16	55,760	55,760	0,495639	0,063756	0,4956	0,0638	0,601E-08	0,851E-09	6,013E-21	0,851E-21

TABLE(A) 2 Data extracted from experiment 16. Sample with H001 configuration, where 10 trials were realized for 4 theta excitation angles, $\theta[^\circ]$, at $B = 5 mT$.

Experiment 16								
Trial	$\theta = 0$		$\theta = -5$		$\theta = -10$		$\theta = -15$	
	$\tau[s]$	$\kappa[N.\mu m^2] \times 10^{-8}$	$\tau[s]$	$\kappa[N.\mu m^2] \times 10^{-8}$	$\tau[s]$	$\kappa[N.\mu m^2] \times 10^{-8}$	$\tau[s]$	$\kappa[N.\mu m^2] \times 10^{-8}$
1	0,4279	0,6540	0,4955	0,5648	0,5817	0,4811	0,5069	0,5521
2	0,5874	0,4764	0,5434	0,5151	0,3488	0,8023	0,4137	0,6765
3	0,6142	0,4556	0,6131	0,4565	0,5592	0,5005	0,44	0,6360
4	0,3767	0,7429	0,3109	0,9002	0,6353	0,4405	0,291	0,9617
5	0,5254	0,5327	0,5605	0,4993	0,585	0,4784	0,4264	0,6563
6	0,5589	0,5007	0,6005	0,4660	0,5828	0,4802	0,2853	0,9809
7	0,2591	1,0808	0,7352	0,3807	0,5697	0,4912	0,3178	0,8806
8	0,5589	0,5007	0,6031	0,4640	0,5915	0,4731	0,4126	0,6783
9	0,5414	0,5169	0,5284	0,5296	0,5326	0,5255	0,3609	0,7754
10	0,5284	0,5296	0,5600	0,4997	0,3975	0,7040	0,458	0,6110

TABLE(A) 3 Summarized data extracted from experiments 6, 13, 14, and 23 with H010 configuration. With length, $L[\mu m]$, relaxation time, $\tau[s]$, and average bending stiffness, $\langle\kappa\rangle[N.m^2]$, and their respective standard deviations.

H010	$L[\mu m]$	$\langle L \rangle[\mu m]$	$\tau[s]$	$\delta\tau[s]$	$\langle\tau\rangle[s]$	$\langle\delta\tau\rangle[s]$	$\kappa[N.\mu m^2]$	$\delta\kappa[N.\mu m^2]$	$\langle\kappa\rangle[N.\mu m^2]$	$\delta\langle\kappa\rangle[N.\mu m^2]$
6	54,500		0,229912	0,079253			1,11E-08	0,951E-09		
13	59,762		0,225051	0,049989	0,2304	0,0175	1,13E-08	2,20E-09	12,27E-21	1,729E-21
14	56,731	57,370	0,206007	0,045248			1,24E-08	2,46E-09		
23	58,487		0,260592	0,019543			1,42E-08	1,30E-09		

TABLE(A) 4 Data extracted from experiment 6. Sample with H010 configuration, where 10 trials were realized for 3 theta excitation angles, θ [°], at $B = 5 \text{ mT}$.

Experiment 6						
Trial	$\theta = 0$		$\theta = -10$		$\theta = -15$	
	τ [s]	$\kappa[\text{N}\cdot\mu\text{m}^2] \times 10^{-8}$	τ [s]	$\kappa[\text{N}\cdot\mu\text{m}^2] \times 10^{-8}$	τ [s]	$\kappa[\text{N}\cdot\mu\text{m}^2] \times 10^{-8}$
1	0,1487	1,916	0,1534	1,723	0,1103	2,890
2	0,0971	2,892	0,0924	2,955	0,1558	1,640
3	0,0707	3,726	0,0846	2,954	0,1193	2,210
4	0,2241	1,202	0,1650	1,438	0,0873	2,580
5	0,1499	1,735	0,1399	1,388	0,1178	2,240
6	0,1876	1,409	0,1286	1,480	0,1625	1,550
7	0,1398	1,812	0,2032	0,796	0,1451	1,750
8	0,2744	0,966	0,1835	1,241	0,1678	1,540
9	0,1729	1,668	0,1243	1,817	0,1553	1,510
10	0,1625	1,766	0,1593	1,196	0,1391	1,540

TABLE(A) 5 Data extracted from experiment 13. Sample with H010 configuration, where 10 trials were realized for 4 theta excitation angles, θ [°], at $B = 5 \text{ mT}$.

Experiment 13								
Trial	$\theta = 0$		$\theta = -5$		$\theta = -10$		$\theta = -15$	
	τ [s]	$\kappa[\text{N}\cdot\mu\text{m}^2] \times 10^{-8}$	τ [s]	$\kappa[\text{N}\cdot\mu\text{m}^2] \times 10^{-8}$	τ [s]	$\kappa[\text{N}\cdot\mu\text{m}^2] \times 10^{-8}$	τ [s]	$\kappa[\text{N}\cdot\mu\text{m}^2] \times 10^{-8}$
1	0,0945	3,8670	0,4461	0,8189	0,2836	1,2883	0,2495	1,4645
2	0,2035	1,7955	0,2286	1,5979	0,4355	0,8389	0,2128	1,7167
3	0,1968	1,8650	0,1039	3,5175	0,3127	1,1684	0,2429	1,5041
4	0,4550	0,8030	0,1098	1,8420	0,2417	1,5113	--	--
5	0,1353	2,6993	0,3439	1,0624	0,3812	0,9583	--	--
6	0,1083	3,3744	0,1409	2,5936	0,0719	5,0811	--	--
7	0,3359	1,0877	0,5290	0,6906	0,2986	1,2236	--	--
8	0,2084	1,7527	0,3281	1,1136	0,4280	0,8536	--	--
9	0,2870	1,2729	0,1186	3,0798	0,3134	1,1657	--	--
10	0,2415	1,5128	0,1055	3,4635	0,1269	2,8787	--	--

TABLE(A) 6 Data extracted from experiment 14. Sample with H010 configuration, where 10 trials were realized for 4 theta excitation angles, θ [°], at $B = 5 \text{ mT}$.

Experiment 14								
Trial	$\theta = 0$		$\theta = -5$		$\theta = -10$		$\theta = -15$	
	τ [s]	κ [N. μm^2] $\times 10^{-8}$	τ [s]	κ [N. μm^2] $\times 10^{-8}$	τ [s]	κ [N. μm^2] $\times 10^{-8}$	τ [s]	κ [N. μm^2] $\times 10^{-8}$
1	0,2442	1,2149	0,1365	2,1732	0,1770	1,6759	0,1443	2,0565
2	0,8095	0,3665	0,3305	0,8977	0,1577	1,8810	0,1937	1,5315
3	0,2777	1,0684	0,6381	0,4650	0,1377	2,1544	0,1591	1,8641
4	0,2348	1,2636	0,9575	0,3098	0,2432	1,1297	0,1158	2,5614
5	0,3334	0,0974	0,1665	1,7817	0,1153	2,5741	0,2118	1,4007
6	0,1598	1,8564	0,1865	1,5903	0,1993	1,4883	0,1995	1,4872
7	0,2314	1,2820	0,1181	2,5115	0,2244	1,3220	0,1854	1,6003
8	0,1045	2,8391	0,2727	1,0879	0,1723	1,7222	0,1438	2,0637
9	0,1919	1,5461	0,2147	1,3819	0,1649	1,7996	0,1546	1,9184
10	0,2098	1,4144	0,1124	2,6403	0,1160	2,5573	0,1625	1,8252

TABLE(A) 7 Data extracted from experiment 23. Sample with H010 configuration, where 8 trials were realized for 3 theta excitation angles, θ [°], at $B = 5 \text{ mT}$.

Experiment 23						
Trial	$\theta = 0$		$\theta = 5$		$\theta = 10$	
	τ [s]	κ [N. μm^2] $\times 10^{-8}$	τ [s]	κ [N. μm^2] $\times 10^{-8}$	τ [s]	κ [N. μm^2] $\times 10^{-8}$
1	0,2886	0,9457	0,1976	1,6959	0,2099	1,5965
2	0,2190	1,2463	0,1405	2,3850	0,2681	1,2502
3	0,1227	2,2247	0,1971	1,7002	0,1575	2,2182
4	0,5307	0,5144	0,2152	1,5577	0,1947	1,7213
5	0,3742	0,7295	0,2496	1,3430	0,2701	1,2409
6	--	--	0,7656	0,4378	0,3695	0,9071
7	0,1550	1,7612	0,2392	1,4010	0,2282	1,4687
8	0,1924	1,4190	0,2419	1,3854	0,1754	1,9106
9	--	--	--	--	--	--
10	0,2515	1,0855	--	--	--	--

TABLE(A) 8 Summarized data extracted from experiments 19 and 20 with H100 configuration. With length, L [μm], relaxation time, τ [s], and average bending stiffness, $\langle\kappa\rangle$ [N. m^2], and their respective standard deviations.

H100	L [μm]	$\langle L \rangle$ [μm]	τ [s]	$\delta\tau$ [s]	$\langle\tau\rangle$ [s]	$\langle\delta\tau\rangle$ [s]	κ [N. μm^2]	$\delta\kappa$ [N. μm^2]	$\langle\kappa\rangle$ [N. μm^2]	$\delta\langle\kappa\rangle$ [N. μm^2]
19	55,562		0,520907	0,049527			0,554E-08	0,421E-09		
20	56,130	55,846	1,419880	0,221070	0,9704	0,1353	0,205E-08	0,335E-09	3,797E-21	0,378E-21

TABLE(A) 9 Data extracted from experiment 19. Sample with H100 configuration, where 10 trials were realized for 1 theta excitation angle, $\theta [^\circ]$, at $B = 5 mT$.

Experiment 19		
Trial	$\theta = 0$	
	$\tau [s]$	$\kappa [N.\mu m^2] \times 10^{-8}$
1	1,4923	0,1905
2	1,5379	0,1849
3	1,6464	0,1727
4	1,3337	0,2132
5	1,4140	0,2011
6	1,7937	0,1585
7	1,1465	0,2480
8	1,2036	0,2362
9	1,5680	0,1813
10	1,0627	0,2675

TABLE(A) 10 Data extracted from experiment 20. Sample with H100 configuration, where 10 trials were realized for 3 theta excitation angles, $\theta [^\circ]$, at $B = 5 mT$.

Experiment 20						
Trial	$\theta = 0$		$\theta = 5$		$\theta = 10$	
	$\tau [s]$	$\kappa [N.\mu m^2] \times 10^{-8}$	$\tau [s]$	$\kappa [N.\mu m^2] \times 10^{-8}$	$\tau [s]$	$\kappa [N.\mu m^2] \times 10^{-8}$
1	0,4453	0,6130	0,6167	0,4462	0,6436	0,4241
2	0,6016	0,4537	0,4717	0,5787	0,3827	0,7133
3	0,5916	0,4614	0,4902	0,5568	0,4271	0,6391
4	0,6249	0,4368	0,4834	0,5646	0,5278	0,5171
5	0,4117	0,6631	0,3712	0,7353	0,3752	0,7275
6	0,5102	0,5350	0,5048	0,5408	0,6739	0,4505
7	0,3765	0,7250	0,4185	0,6523	0,6100	0,4475
8	0,5603	0,4872	0,4954	0,5510	0,5594	0,4880
9	0,8927	0,3058	0,3787	0,7207	0,5638	0,4814
10	0,8173	0,3340	0,3898	0,7002	0,4112	0,6687

TABLE(A) 11 Summarized data extracted from experiments 4, 11, 12, and 20 with H011 configuration. With length, $L [\mu m]$, relaxation time, $\tau [s]$, and average bending stiffness, $\langle \kappa \rangle [N.m^2]$, and their respective standard deviations.

H011	$L [\mu m]$	$\langle L \rangle [\mu m]$	$\tau [s]$	$\delta \tau [s]$	$\langle \tau \rangle [s]$	$\langle \delta \tau \rangle [s]$	$\kappa [N.\mu m^2]$	$\delta \kappa [N.\mu m^2]$	$\langle \kappa \rangle [N.\mu m^2]$	$\delta \langle \kappa \rangle [N.\mu m^2]$
4	52,253		0,122919	0,06187			1,78E-08	2,26E-09		
11	55,668		0,116063	--			2,47E-08	4,51E-09		
12	45,821	52,778	0,130780	--	0,1528	0,1048	0,999E-08	1,65E-09	15,86E-21	2,741E-21
15	57,371		0,241487	0,14777			1,09E-08	2,55E-09		

TABLE(A) 12 Data extracted from experiment 4. Sample with H011 configuration, where 10 trials were realized for 3 theta excitation angle, $\theta[^\circ]$, at $B = 5 \text{ mT}$.

Experiment 4						
Trial	$\theta = 0$		$\theta = -10$		$\theta = -20$	
	$\tau[s]$	$\kappa[N.\mu m^2] \times 10^{-8}$	$\tau[s]$	$\kappa[N.\mu m^2] \times 10^{-8}$	$\tau[s]$	$\kappa[N.\mu m^2] \times 10^{-8}$
1	0,0858	2,490	0,1103	1,937	0,1225	1,743
2	0,1225	1,743	0,1348	1,584	0,1225	1,743
3	0,0980	2,179	0,1225	1,743	0,1470	1,452
4	0,1103	1,937	0,1470	1,452	0,0980	2,179
5	0,1225	1,743	0,1225	1,743	0,1225	1,743
6	0,0858	2,490	0,1470	1,452	0,1470	1,452
7	0,1225	1,743	0,1103	1,937	0,1470	1,452
8	0,1225	1,743	0,1348	1,584	0,1470	1,452
9	0,0858	2,490	0,1225	1,743	0,1348	1,584
10	0,1348	1,584	0,1225	1,743	0,1348	1,584

TABLE(A) 13 Data extracted from experiment 15. Sample with H011 configuration, where 10 trials were realized for 4 theta excitation angle, $\theta[^\circ]$, at $B = 5 \text{ mT}$.

Experiment 15								
Trial	$\theta = 0$		$\theta = -5$		$\theta = -10$		$\theta = -15$	
	$\tau[s]$	$\kappa[N.\mu m^2] \times 10^{-8}$	$\tau[s]$	$\kappa[N.\mu m^2] \times 10^{-8}$	$\tau[s]$	$\kappa[N.\mu m^2] \times 10^{-8}$	$\tau[s]$	$\kappa[N.\mu m^2] \times 10^{-8}$
1	0,4716	0,6580	0,3618	0,8577	0,3099	1,0012	0,4584	0,6769
2	0,4159	0,7461	0,3686	0,8418	0,2979	1,0416	0,1654	1,8756
3	0,4700	0,6602	0,3907	0,7942	0,1857	1,6707	0,1611	1,9257
4	0,3488	0,8896	0,2251	1,3783	0,2037	1,5235	0,1201	2,5836
5	0,3846	0,8069	0,3297	0,9411	0,2787	1,1133	0,2517	1,2330
6	0,4671	0,6643	0,2742	1,1318	0,2272	1,3658	0,2981	1,0409
7	0,3735	0,8308	0,3006	1,0322	0,2802	1,1073	0,2150	1,4431
8	0,4333	0,7161	0,2782	1,1155	0,3314	0,9362	0,1923	1,6136
9	0,3255	0,9533	0,3289	0,9435	0,3962	0,7832	0,3437	0,9027
10	0,5389	0,5758	0,2511	1,2359	0,3398	0,9132	0,2504	1,2390

TABLE(A) 14 Summarized data extracted from experiments 8 and 24 with H101 configuration. With length, $L[\mu m]$, relaxation time, $\tau[s]$, and average bending stiffness, $\langle \kappa \rangle [N.m^2]$, and their respective standard deviations.

H101	$L[\mu m]$	$\langle L \rangle [\mu m]$	$\tau[s]$	$\delta\tau[s]$	$\langle \tau \rangle [s]$	$\langle \delta\tau \rangle [s]$	$\kappa[N.\mu m^2]$	$\delta\kappa[N.\mu m^2]$	$\langle \kappa \rangle [N.\mu m^2]$	$\delta\langle \kappa \rangle [N.\mu m^2]$
8	49,985	51,894	0,388165	0,030518	0,2859	0,0171	0,465E-08	0,395E-09	9,39E-21	0,418E-21
24	53,803		0,183659	0,003679			1,41E-08	0,442E-09		

TABLE(A) 15 Data extracted from experiment 8. Sample with H101 configuration, where 10 trials were realized for 1 theta excitation angle, $\theta[^\circ]$, at $B = 5 \text{ mT}$.

Experiment 8		
Trial	$\theta = 0$	
	$\tau[s]$	$\kappa[N.\mu m^2] \times 10^{-8}$
1	0,3430	1,747
2	0,3430	1,747
3	0,3675	1,631
4	0,3675	1,631
5	0,3553	1,687
6	0,3675	1,631
7	0,4043	1,482
8	0,3920	1,529
9	0,4288	1,398
10	0,4288	1,398

TABLE(A) 16 Data extracted from experiment 24. Sample with H101 configuration, where 10 trials were realized for 3 theta excitation angle, $\theta[^\circ]$, at $B = 5 \text{ mT}$.

Experiment 24						
Trial	$\theta = 0$		$\theta = 5$		$\theta = 10$	
	$\tau[s]$	$\kappa[N.\mu m^2] \times 10^{-8}$	$\tau[s]$	$\kappa[N.\mu m^2] \times 10^{-8}$	$\tau[s]$	$\kappa[N.\mu m^2] \times 10^{-8}$
1	0,1576	1,5234	0,2116	1,1342	0,2033	1,1803
2	0,1291	1,8598	0,1356	1,7700	0,1216	1,9735
3	0,1215	1,9761	0,2125	1,1297	0,1613	1,4878
4	0,1570	1,5290	0,1519	1,5796	0,2081	1,1532
5	0,2556	0,9389	0,1132	2,1206	0,1463	1,6403
6	0,1072	2,2384	0,2094	1,1461	0,1983	1,2106
7	0,2781	0,8629	0,1752	1,3701	0,1837	1,3065
8	0,3108	0,7723	0,2209	1,0864	0,2391	1,0038
9	0,1359	1,7664	0,1534	1,5648	--	--
10	0,2242	1,0705	--	--	0,1986	1,2085

TABLE(A) 17 Summarized data extracted from experiments 18 and 22 with H110 configuration. With length, $L[\mu m]$, relaxation time, $\tau[s]$, and average bending stiffness, $\langle \kappa \rangle [N.m^2]$, and their respective standard deviations.

H110	$L[\mu m]$	$\langle L \rangle [\mu m]$	$\tau[s]$	$\delta\tau[s]$	$\langle \tau \rangle [s]$	$\langle \delta\tau \rangle [s]$	$\kappa[N.\mu m^2]$	$\delta\kappa[N.\mu m^2]$	$\langle \kappa \rangle [N.\mu m^2]$	$\delta\langle \kappa \rangle [N.\mu m^2]$
18	57,250	57,075	1,180010	0,230650	0,7849	0,1390	0,27E-08	0,472E-09	5,346E-21	0,743E-21
22	56,900		0,389825	0,047292			0,80E-08	1,01E-09		

TABLE(A) 18 Data extracted from experiment 18. Sample with H110 configuration, where 10 trials were realized for 1 theta excitation angle, $\theta[^\circ]$, at $B = 5 mT$.

Experiment 18		
Trial	$\theta = 0$	
	$\tau[s]$	$\kappa[N,\mu m^2] \times 10^{-8}$
1	1,2987	0,2368
2	1,7531	0,1755
3	1,0964	0,2805
4	1,0525	0,2922
5	1,1362	0,2707
6	1,1873	0,2591
7	0,9350	0,3289
8	0,8678	0,3544
9	1,2499	0,2461
10	1,2232	0,2515

TABLE(A) 19 Data extracted from experiment 22. Sample with H110 configuration, where 3 and 6 trials were realized for 2 theta excitation angle, $\theta[^\circ]$, at $B = 5 mT$.

Experiment 22				
Trial	$\theta = 0$		$\theta = 10$	
	$\tau[s]$	$\kappa[N,\mu m^2] \times 10^{-8}$	$\tau[s]$	$\kappa[N,\mu m^2] \times 10^{-8}$
1	0,4110	0,7306	0,5445	0,5514
2	0,2739	1,0962	0,4598	0,6531
3	0,3427	0,8763	0,4484	0,6697
4	--	--	0,3685	0,8148
5	--	--	0,4186	0,7173
6	--	--	0,3829	0,7842
7	--	--	--	--
8	--	--	--	--
9	--	--	--	--
10	--	--	--	--

TABLE(A) 20 Summarized data extracted from experiments 3, 5, 7, and 17 with H111 configuration. With length, $L[\mu m]$, relaxation time, $\tau[s]$, and average bending stiffness, $\langle \kappa \rangle [N \cdot m^2]$, and their respective standard deviations.

H111	$L[\mu m]$	$\langle L \rangle [\mu m]$	$\tau[s]$	$\delta\tau[s]$	$\langle \tau \rangle [s]$	$\langle \delta\tau \rangle [s]$	$\kappa[N,\mu m^2]$	$\delta\kappa[N,\mu m^2]$	$\langle \kappa \rangle [N,\mu m^2]$	$\delta\langle \kappa \rangle [N,\mu m^2]$
3	50,494		0,0747315	0,038096			2,5924E-08	4,27E-09		
5	58,236		0,2839185	0,083214			1,2144E-08	2,20E-09		
7	46,822	54,071	0,1778061	--	0,2580	0,0465	0,9905E-08	2,11E-09	16,61E-21	2,540E-21
17	60,730		0,4956388	0,018240			1,8480E-08	1,58E-09		

TABLE(A) 23 Data extracted from experiment 3. Sample with H111 configuration, where 10 trials were realized for 5 theta excitation angle, $\theta[^\circ]$, at $B = 5 mT$.

Experiment 3										
Trial	$\theta = 10$		$\theta = 0$		$\theta = -10$		$\theta = -20$		$\theta = -30$	
	$\tau[s]$	$\kappa[N,\mu m^2] \times 10^{-8}$	$\tau[s]$	$\kappa[N,\mu m^2] \times 10^{-8}$	$\tau[s]$	$\kappa[N,\mu m^2] \times 10^{-8}$	$\tau[s]$	$\kappa[N,\mu m^2] \times 10^{-8}$	$\tau[s]$	$\kappa[N,\mu m^2] \times 10^{-8}$
1	0,0613	3,040	0,0858	2,171	0,0735	2,533	0,0735	2,533	0,0721	2,769
2	0,0490	3,800	0,0735	2,533	0,0858	2,171	0,0858	2,171	0,0519	3,588
3	0,0613	3,040	0,0858	2,171	0,0735	2,533	0,0735	2,533	0,0885	2,319
4	0,0490	3,800	0,0613	3,040	0,0980	1,900	0,0980	1,900	0,0727	2,941
5	0,0613	3,040	0,1103	1,689	0,0735	2,533	0,0735	2,533	0,0879	2,162
6	0,0735	2,533	0,0735	2,533	0,0613	3,040	0,0613	3,040	0,0593	3,222
7	0,0858	2,171	0,0613	3,040	0,0735	2,533	0,0735	2,533	0,0586	3,820
8	0,0613	3,040	0,0980	1,900	0,0858	2,171	0,0858	2,171	0,0656	2,932
9	0,0613	3,040	0,0858	2,171	0,0980	1,900	0,0980	1,900	0,0663	3,162
10	0,0490	3,800	0,0613	3,040	0,0858	2,171	0,0858	2,171	0,0680	2,997

TABLE(A) 22 Data extracted from experiment 5. Sample with H111 configuration, where 10 trials were realized for 4 theta excitation angle, $\theta[^\circ]$, at $B = 5 mT$.

Experiment 5									
Trial	$\theta = 0$		$\theta = -10$		$\theta = -20$		$\theta = -30$		
	$\tau[s]$	$\kappa[N,\mu m^2] \times 10^{-8}$	$\tau[s]$	$\kappa[N,\mu m^2] \times 10^{-8}$	$\tau[s]$	$\kappa[N,\mu m^2] \times 10^{-8}$	$\tau[s]$	$\kappa[N,\mu m^2] \times 10^{-8}$	
1	0,1711	1,130	0,1395	1,270	0,1282	1,370	0,0551	3,250	
2	0,0681	2,630	0,1230	1,510	0,2610	0,724	0,1173	1,490	
3	0,0953	1,860	0,1243	1,610	0,1849	0,944	0,0847	2,040	
4	0,1101	1,690	0,1672	1,130	0,1885	0,948	0,0898	1,900	
5	0,1830	1,060	0,07992	2,420	0,2369	0,82	0,1676	1,010	
6	0,0676	2,740	0,1183	1,480	0,2685	0,688	0,1189	1,480	
7	0,1002	1,870	0,1327	1,430	0,1772	0,981	0,0950	1,750	
8	0,2255	0,792	0,0693	2,650	0,2343	0,749	0,0949	1,790	
9	0,1901	1,0	0,0814	2,350	0,2387	0,738	0,1268	1,380	
10	0,1675	1,130	0,1124	1,520	0,2105	0,862	0,1396	1,260	

TABLE(A) 21 Data extracted from experiment 17. Sample with H111 configuration, where 10 trials were realized for 3 theta excitation angle, $\theta[^\circ]$, at $B = 5 mT$.

Experiment 17						
Trial	$\theta = 0$		$\theta = 5$		$\theta = 10$	
	$\tau[s]$	$\kappa[N,\mu m^2] \times 10^{-8}$	$\tau[s]$	$\kappa[N,\mu m^2] \times 10^{-8}$	$\tau[s]$	$\kappa[N,\mu m^2] \times 10^{-8}$
1	0,1604	2,4550	0,1911	2,0606	0,2660	1,4804
2	0,2370	1,6615	0,2450	1,6073	0,2068	1,9041
3	0,1720	2,2894	0,3192	1,2336	0,2010	1,9591
4	0,1839	2,1413	0,2550	1,5442	0,2367	1,6636
5	0,2423	1,6252	0,2281	1,7263	0,1271	3,0982
6	0,2635	1,4944	0,2500	1,5751	0,2269	1,7355
7	0,1997	1,9718	0,2280	1,7271	0,2215	1,7778
8	0,1876	2,0990	0,1959	2,0101	0,1758	2,2399
9	0,2646	1,4882	0,2417	1,6292	0,2683	1,4677
10	0,1389	2,8350	0,3253	1,2105	0,2276	1,7301